ORIGINAL ARTICLE
Journal Section

Sensitivity of tidal hydrodynamics to varying bathymetric configurations in a multi-inlet rapidly eroding salt marsh system: A numerical study

Mithun Deb[1] | Ali Abdolali[2,3,4] | James T. Kirby[1] | Fengyan Shi[1] | Susan Guiteras[5] | Conor McDowell[6]

[1]Center for Applied Coastal Research, Department of Civil and Environmental Engineering, University of Delaware, Newark, DE 19716 USA.

[2]NWS/NCEP/Environmental Modeling Center, National Oceanic and Atmospheric Administration (NOAA), College Park, MD 20740 USA.

[3]I.M. Systems Group, Inc. (IMSG), Rockville, MD 20852 USA.

[4]University of Maryland, College Park, MD 20742, USA

[5]U.S. Fish and Wildlife Service, Coastal Delaware National Wildlife Refuge (NWR) Complex, Smyrna, DE, USA.

[6]Department of Geography, University of British Columbia, Vancouver, V6T 1Z2, BC, Canada.

Correspondence
Mithun Deb, Marine and Coastal Research Laboratory, Coastal Sciences Division, Pacific Northwest National Laboratory
Email: mithun.deb@pnnl.gov

Funding information
National Fish and Wildlife Foundation and the US Department of the Interior, University of Delaware, Grant/Award Number: 43752; Delaware Sea Grant program, University of Delaware, Grant/Award Number: R/HCE-22 and RRCE-12

We describe the development of a high resolution, two-dimensional hydrodynamic model for a multi-inlet rapidly eroding tidal wetland on the western shore of Delaware Bay, using the Finite-Volume, primitive equation Community Ocean Model (FVCOM). Topo-bathymetric surveys, together with water surface and current velocity measurements during calm and stormy conditions, have been conducted to support model validation. The tested model is then used to quantify the tide-induced residual transport and asymmetry at major inlet entrances to determine the governing hydrodynamics. We chose a skewness method to calculate the tidal asymmetry and serve as a proxy for sediment transport estimates. The effects of the dredging of an artificial entrance channel and progressive channel deepening in shifting wetland hydrodynamics are shown by developing a scenario analysis. Model results show that the artificially dredged channel has altered the volume exchange at other inlet entrances and increased the net seaward export. The changes in the characteristic frequency of the frictional dissipation in the channel and the system's natural frequency are investigated using a simple ocean-inlet-bay analytical model. Subsequently, we have compared the channel friction scale to the inertia scale and observed that the new connection and gradual channel deepening reduces the overall frictional dominance. Ultimately, the study has shown how the short and long-term channel bathymetry changes, mainly the artificially dredged channel and progressive channel deepening, can affect the connected system's net circulation and trigger internal marsh erosion.

KEYWORDS

Coastal wetlands, Salt marsh erosion, Tidal Hydrodynamics, Numerical modeling, Channel morphology, Wetland inlet asymmetry

1 | INTRODUCTION

Coastal wetlands provide important ecosystem services such as protecting coastal areas from storm damage and sea level rise, and providing refuge and breeding ground for migrating shorebirds, waterfowl, and other wildlife. The National Oceanic and Atmospheric Administration (NOAA) and the U.S. Fish and Wildlife Service (USFWS) analyzed the status and trends of wetland acreage along the Atlantic Coast, Gulf of Mexico, and the Great Lakes and reported that 361,000 acres of coastal wetlands were lost in the Eastern United States alone between 1998 and 2004 (Stedman and Dahl, 2008). Historically, the Mid-Atlantic region has lost coastal wetlands due to the variety of commercial, residential, and industrial activities as well as conversion for agricultural uses (EPA, 2010). Tidal wetland studies using historical imageries have reported significant marsh degradation in the Chesapeake and Delaware Bay regions (Kearney et al., 2002), in New York City (Hartig et al., 2002), along the Long Island shore (Bowman, 2014), and southern New England (Watson et al., 2017). They have highlighted the role of different anthropogenic and natural processes such as sea-level rise, artificial morphology changes, and marsh overgrazing by native and migratory species on the overall decline. Construction of levees and canals have changed the course of tidal inundation in many coastal wetlands, and led to marsh habitat alteration and destruction (Williams, 1995). During large storm events, wetland systems are often affected by storm surge and waves, where storm induced breaching changes the ocean-inlet-bay dynamics and volume exchange (Aretxabaleta et al., 2017). In the state of Delaware, along Delaware River, numerous breaches were recorded over the last century from historical storms that caused dramatic changes in the wetland ecosystems (Ramsey and Reilly, 2002; Runion, 2019). The Bombay Hook National Wildlife Refuge (BHNWR), DE is one of the largest remaining expanses of tidal wetlands in the mid-Atlantic region and has lost almost 20% of its salt marsh area since 1949 (Figure 1). Over the years, this multi-inlet salt marsh system has gone through a combination of anthropogenic (Dozier, 1947) and natural changes (Ramsey and Reilly, 2002), shifting its tidal dynamics from time to time.

Coastal wetland morphology and tidal processes are interdependent on each other. An abrupt change in estuarine morphology caused by any anthropogenic or natural process could affect the hydrodynamics, which in turn alter the evolution of the estuary (Speer, 1984; Dronkers, 1986). The net residual sediment transport in a system is related to tidal asymmetry and phase difference between surface elevation and flow velocity (Hsu et al., 2013; Ralston et al., 2013). The hydrodynamic regime, including asymmetry in the system (i.e., flood/ebb dominance during spring/neap tide) and inter-tidal storage controls the net volume exchange, residual volume transport and overall stability of a tidal wetland (Aubrey and Speer, 1985; Speer et al., 1991; Rinaldo et al., 1999; Friedrichs, 2010; Nardin et al., 2020). Various coastal wetlands/lagoons around the world such as the Venice Lagoon, Italy (Donda et al., 2008; Ferrarin et al., 2015) and Ria de Aveiro, Portugal (Picado et al., 2010) are reported to show changes in tidal asymmetry from human interventions. These cases have shown an increase in ebb dominance and erosion over the years from channel dredging for navigational purposes. The tidal asymmetry can be represented in several ways such as (1) by duration asymmetry, which measures the difference in duration between rising and falling tide, and (2) using velocity skewness that characterizes the ebb and flood current distribution over a tide cycle (Nidzieko and Ralston, 2012). The duration asymmetry is controlled by the variation in channel volume and the intertidal volume of adjacent shoals (Speer, 1984; Friedrichs, 2010), and the velocity skew can generate from the local bathymetry gradients, quadratic friction and the phase lags between the surface gradient and local depth (Nidzieko and Ralston, 2012). Also, tidal wetlands with multiple inlets can have complicated circulation patterns due to the internal connections between the channel entrances that can affect the overall asymmetry (Orescanin et al., 2016). The difference in slack water period between ebb and flood (when there is no horizontal motion) generally affects the residual flux of the fine suspended load, while the difference between maximum tidal currents particularly affects the bed load transport (Dronkers, 1986). Besides the channel sediment transport, the tidal flow properties are also essential for the salt marsh vegetation dynamics.

The coastal salt marsh stability depends on the tidal range, the marsh platform's elevation, weather variability, and vegetation biomass (Kirwan and Murray, 2007; Mudd et al., 2013). The vegetation biomass growth rate depends on tidal amplitude, period, and local elevation, resulting in different vegetation species dominating different zones. Tidal current suspends sediment from the mudflat and channel bottom and transports it to the marsh platform. Marsh vegetation interacts with sediment dynamics as it traps the transported materials during different tidal conditions, finally modifying the landscape (Mariotti and Fagherazzi, 2010). In recent studies, Kirwan and Guntenspergen (2010) and Watson et al. (2017) have shown that the coastal marshland stability is a function of tidal range; and the shifts in the hydroperiod can lead to formations of depression and ponds, ultimately leading to more significant marsh loss.

As the coastal wetlands are among the most economically important ecosystems on Earth, it is essential to better understand the critical tidal processes responsible for triggering internal marsh erosion and wetland instability. Specifically, having a greater understanding of the impact of artificial bathymetry changes on tidal dynamics in complex multi-inlet systems can provide us valuable insights into net sediment transport changes and the overall erosion/accretion. This paper examines the effects of artificial dredged entrance channels and changes in channel bathymetry in shifting the wetland interior tidal range and inlet volume exchange and asymmetry. We chose BHNWR, DE, as a study site, crucial for the ecology and economy of the Delaware coastal environment, and has been through significant morphology changes over the years due to direct human modification. The main objective of the work is to evaluate how the short and long-term historical morphology changes: the artificial channel opening and progressive channel deepening with time, respectively, can alter the tidal hydrodynamics and contribute to marsh-channel erosion and wetland loss. We developed a high-resolution two-dimensional model system for the entire BHNWR tidal wetland environment based on the Finite-Volume, primitive equation Community Ocean Model (FVCOM, Chen et al. (2013)). The unstructured grid developed for BHNWR covers the entire marsh system with sufficient grid resolution to resolve small channels and creeks. The model is validated using surface elevations at several tidal gauges and the ADCP current velocity data. Model performance for predicting flooding/draining processes during normal and storm conditions has been examined using the data collected on the marsh platform. For the severe surge condition, two extreme meteorological events that threatened Delaware Bay with storm surge and large-scale coastal flooding, Hurricane Sandy (2012) and Hurricane Joaquin (2015) (Dohner et al., 2016), were selected. After extensive model validation, we use the model output, mainly the water surface elevation and depth-averaged current velocity, to examine tidal asymmetry and flow exchange in the marsh's multiple entrance channels. A statistical skewness method is used for tidal asymmetry calculations, which also provided some relevant metrics for sediment transport. Finally, a channel bathymetry scenario analysis is developed based on the historical changes in the system to evaluate the shifts in tidal hydrodynamics. These hydrodynamic results are then used to establish a relation between the changes in tidal dynamics and subsequent marsh erosion, which can be insightful for the coastal wetland community.

This paper is organized as follows. The historical changes in the system is presented in Section 2. Section 3 describes the model grid and Digital Elevation Model (DEM) development, model validation with field data, and the method used for asymmetry calculation. Scenario development with present-day bathymetry and morphology changes is provided in Section 4, and Section 5 discusses the tidal processes' response to the applied scenarios. The corresponding changes in the system's frictional dominance and sediment transport mechanism are described in section 6. Concluding remarks and observations on needed future work are given in section 7.

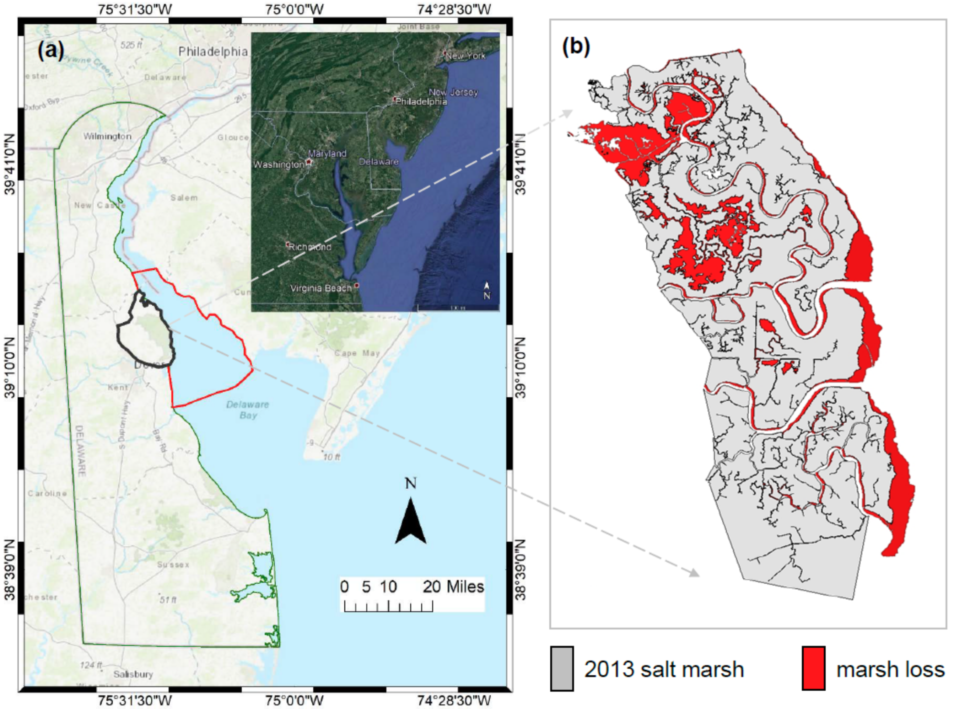

FIGURE 1 (a) Bombay Hook National Wildlife Refuge, DE. Red and black polygons show the model outer boundaries in Bay and BHNWR respectively; (b) Marsh loss between 1949 and 2013. Grey area shows the existing salt marsh while the marsh platform loss since 1949 is shown in red (panel (b) taken from McDowell and Sommerfield (2016)).

2 | REGIONAL DESCRIPTION

The BHNWR wetland system originally had three natural tidal inlets, the Leipsic River, Simons River, and the Woodland Beach inlet (Figure 2a). A new channel, Sluice Ditch, was constructed in 1890 to connect the marsh interior at Duck Creek directly to Delaware Bay (Dozier, 1947). Additionally, several oxbows in the Leipsic River course were straightened before and during 1900, which changed the drainage system of wet areas (Dozier, 1947; Ramsey and Reilly, 2002). Over the 100 year period, the main channels of the system have progressively deepened and widened. Cross-section averaged depth, which was close to 4.0-5.0m along the major channels (United States. Army. Corps of Engineers, 1910), is now almost 10.0 m at some locations, and the width has more than doubled and reached approximately 100.0 m in Sluice Ditch. From the comparison of historical imagery of 1968 and 2002 in Figure 3, we can also see that the system has different trends in the upper and lower regions. In one part, three of the inlets, Leipsic River, Sluice Ditch, and Woodland Beach, are connected by the major channels. We consider this region the disturbed region, where the interior marsh surface has collapsed extensively and formed tidal mudflats. On the lower side, the Simons River inlet is mostly separated from the system and has less overall erosion, described as undisturbed part (Figure 3, right subplot). In addition to internal marsh and channel erosion, the marsh shoreline with the Delaware Bay has also experienced significant wave-driven erosion over the years (Chen et al., 2018).

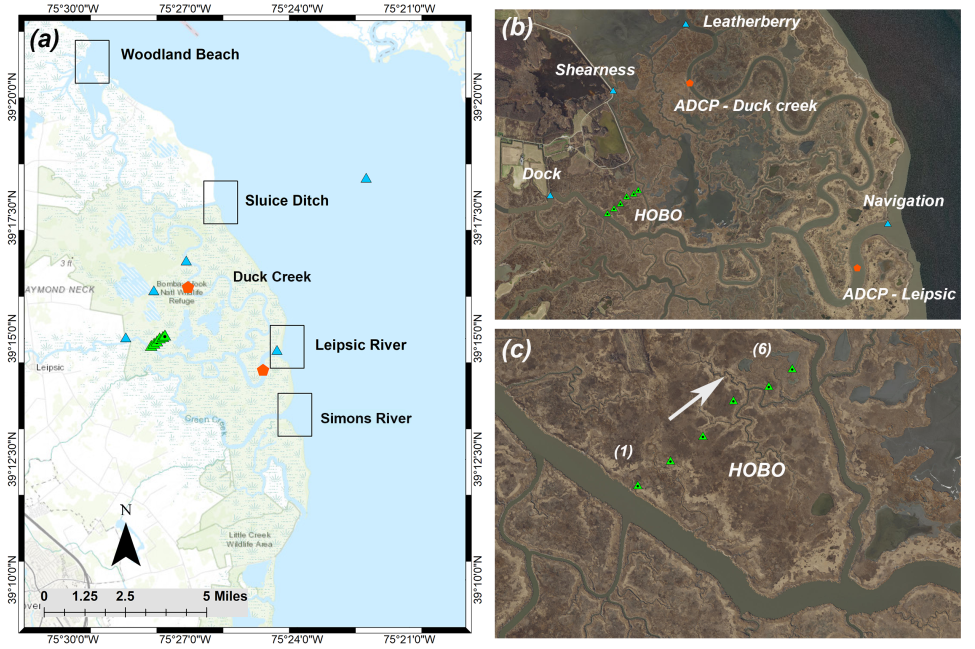

FIGURE 2 (a) Leipsic River, Simons River, Sluice Ditch/Duck Creek and Woodland Beach inlets that connect BHNWR wetland system with the Delaware estuary and Bay. The total volume flux going in/out of the system are estimated later using these four inlets. HOBO pressure gauges, DNREC tide gauges inside the wetland and NOAA gauge in the Bay, and ADCP locations used for the model validation are shown in green triangles, blue triangles and orange pentagons; (b) Similar gauges are shown with more description; (c) A closer look to the HOBO pressure gauge locations.

3 | METHOD

3.1 | Model setup and validation

FVCOM solves primitive governing equations for momentum, incompressible volume, temperature, salinity and density. The momentum equations are solved using a mode-splitting method, in which an external, barotropic mode solves 2D depth-integrated equations, and an internal, baroclinic mode solves the equations in three dimensions. This model has been previously used in several estuarine and coastal studies featuring complex topo-bathymetry, inter-tidal wetting and drying, and irregular coastline (Chen et al., 2008). Huang et al. (2008) used FVCOM 3D successfully to analyze estuarine processes and tidal asymmetry in Okatee Creek, South Carolina. Similarly, Ralston et al. (2013) validated FVCOM using field data and investigated hydrodynamics and sediment transport on deltaic tidal flats at the mouth of the Skagit River, in Puget Sound, WA. Developing a reliable high-resolution three-dimensional salt marsh model is challenging due to numerical instabilities from extreme thin-layer flows over the marsh surface and sharp bathymetry gradients around the marsh-channel boundaries, and it is still a matter of active research (Li and Hodges, 2019). For this study we used the 2D (vertically integrated) FVCOM to avoid the model numerical instability from extreme shallow conditions over the marsh surface during both wetting and drying.

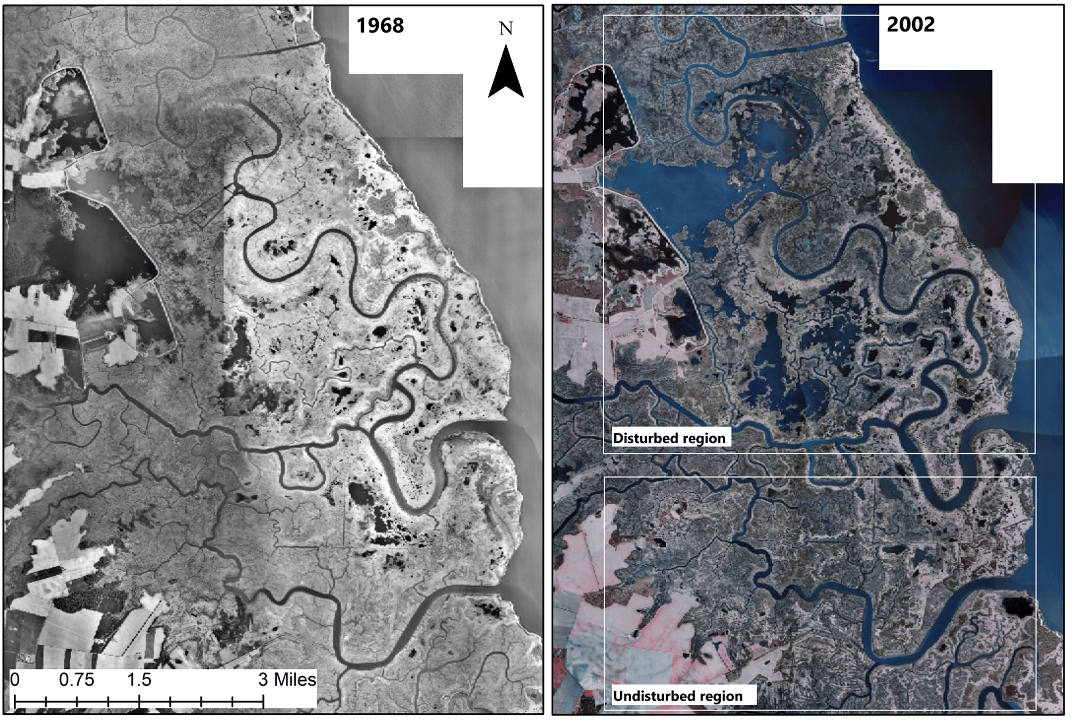

FIGURE 3 BHNWR internal marsh loss: comparison between 1968 and 2002 aerial images show the rate of the ongoing erosion. Aerial photographs collected from the repository of Delaware Environmental Monitoring & Analysis Center (http://demac.udel.edu/data/aerial-photography/).

3.1.1 | Unstructured grid development

The domain for the numerical simulation covers an area similar to that used by Stammerman (2013) for a previous hydrodynamic study of the same area. The model grid domain shown in Figure 4a covers Delaware Bay from Bowers, DE on the southern boundary up to 39° 25′ N latitude in Delaware River. The grid is extended landward on the western shore of the bay to cover the entire BHNWR wetland. Grid resolution in marsh-channel boundaries are as fine as ~ 3 m in order to resolve channels and channel berm geometry. We have collected three high resolution LiDAR data sets of the years 2007, 2011 and 2014 from different sources (Deb et al., 2018a) and processed to a regular grid with 1 m in resolution to represent the study area. After comparing them with the surveyed marsh ground elevation, we selected the most accurate one, of the year 2011, and further corrected the bias based on surveyed vegetation type data along random transects in different wetland locations. Interestingly, from the comparison between LiDAR and field survey, we observed an uniform bias distribution of 0.1 m for locations representing high marshes and close to 0.2 m for low marshes in the LiDAR DEM. The DEM is then readjusted considering these two sets of errors and ultimately interpolated to the model unstructured grid nodes. Bathymetric surveys of the main waterways in BHNWR were conducted to obtain continuous depth soundings of the bottom below tide level. The data was de-tided using the nearest tide-gauge location Dock and the soundings were converted to the NAVD88 datum for gridding with LiDAR data. The detailed description of the LiDAR source and accuracy, DEM comparison with the ground truth survey, vegetation bias correction, channel survey and pre/post processing of the data set can be found in Deb et al. (2018a) and Deb et al. (2018b).

3.1.2 | Model forcing

The FVCOM unstructured grid with refinement in BHNWR area is driven by surface elevation and flux information at upstream and downstream boundary nodes, extracted from a larger-scale implementation of the ROMS/COAWST model (Rodrigues, 2016; Kukulka et al., 2017). Simulations were conducted for the years of 2012 and 2015 (Kukulka et al., 2017; Rodrigues, 2016). ROMS simulations were performed on a regular curvilinear grid covering Delaware Bay and extending offshore to the 100m isobath (Figure 4a). The ROMS grid has a maximum resolution of 0.75-2.0 km near the bay mouth, with lower grid resolution of about 8 km near the shelf break. The model used ten layers to resolve vertical structure. The ocean model was driven with nine dominant tidal constituents (M2, S2, M4, M6, K2, K1, N2, O1, and Q1) imposed from the ADCIRC database (Luettich Jr et al., 1992). Atmospheric pressure and wind forcing were taken from the North American Mesoscale model (NAM) (`nomads.ncdc.noaa.gov`). Delaware River discharge data was obtained based on the USGS gauge at Trenton, New Jersey (`waterdata.usgs.gov`). Results are compared against NOAA tide gauges located in the Bay (`tidesandcurrents.noaa.gov`), with results for one gauge location (Ship John Shoal, `https://tidesandcurrents.noaa.gov/ports/ports.html?id=8537121`), closest to the study area, shown here for illustration (Figure 5). From Figure 5, it can be clearly seen that ROMS predicts tidal harmonics accurately (second panel) and underestimates the sub-tidal signal (third panel) at the Ship John Shoal gauge. It is caused by the missing remote forcing at the ROMS upstream boundary close to Mid-New Jersey (Figure 4a). To properly represent surface elevation at the FVCOM boundary, we separated the elevation data from ROMS into tidal and sub-tidal signals using T_TIDE (Pawlowicz et al., 2002). Then, we applied the same procedure to publicly available NOAA tide gauge datasets from Reedy Point, DE; Ship John Shoal, NJ and Bower, DE in the Delaware Bay (`tidesandcurrents.noaa.gov`), and observed a similar trend in their sub-tidal signals. Finally, we have superimposed the ROMS tidal harmonics at the FVCOM boundary nodes with in-situ sub-tidal data from NOAA tide gauges near boundary nodes. Meanwhile, we kept the volume flux information from ROMS unchanged at the FVCOM boundary nodes.

In FVCOM, it is possible to implement three different nesting conditions at the boundary, denoted as "direct nesting", "indirect nesting" and "relaxing nesting". We used the "direct nesting" approach in FVCOM, which allows nesting between small domain FVCOM and large domain ROMS with corrected sub-tidal data and volume flux at open boundary nodes, shown in Figure 4b and 4c. Lateral mixing in FVCOM is computed using the Smagorinsky scheme with a horizontal diffusion coefficient of 0.2 m^2/s. We used a Manning's Roughness Coefficient of $n = 0.02$ to estimate the drag coefficient C_d, and a minimum depth $5cm$ for model wetting/drying. The Manning's coefficient is given as a universal number; however, we limited the minimum drag coefficient C_d value to 0.0025 at higher depths at the channels and Bay. Over the marsh surface and shallow regions, we have a more significant drag coefficient than 0.0025 due to the smaller water depth.

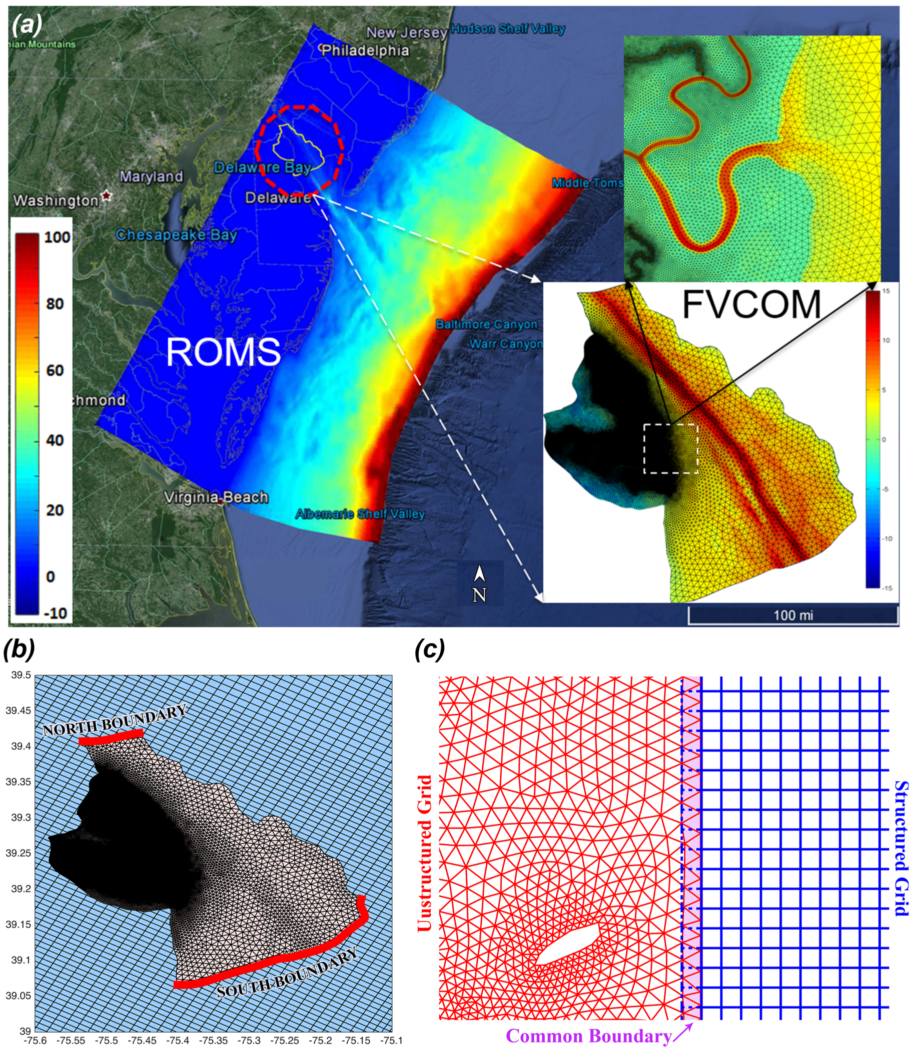

FIGURE 4 Models coupling scheme; (a) structured ROMS numerical domain covering Delaware Bay extended to the continental shelf in Atlantic ocean and unstructured FVCOM domain. The grid depth is shown in meters, from NAVD88 vertical reference level; (b) Schematic view of data exchange between ROMS and FVCOM at common boundary nodes at upstream and downstream side of the Delaware Bay; (c) Schematic view of FVCOM direct nesting at the boundary nodes.

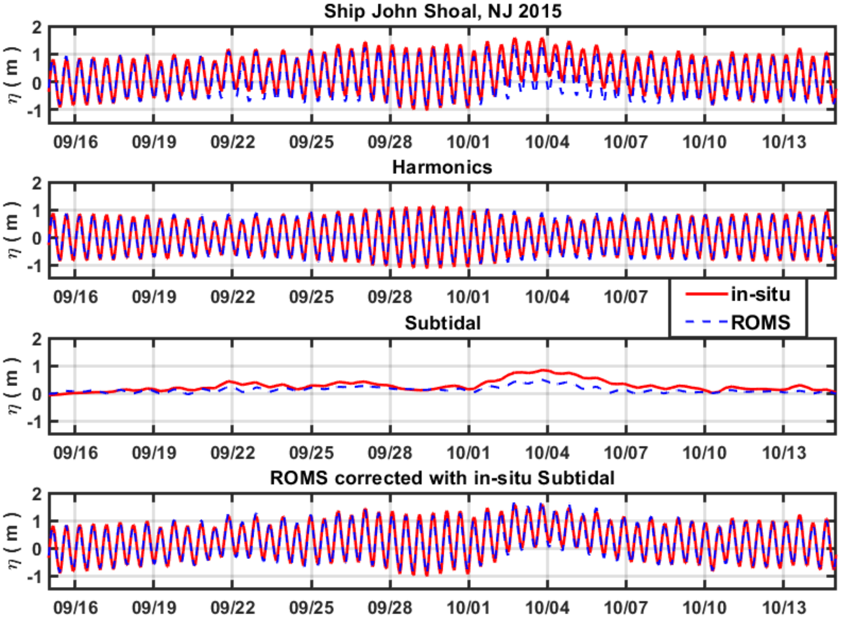

FIGURE 5 Comparison of in-situ (red) and ROMS outputs (blue) in term of free surface elevation at Ship John Shoal, Delaware Bay (2015); Pre-processed signals (top), tidal harmonics (second panel), subtidal (third panel) and subtidal corrected (lower panel) signal.

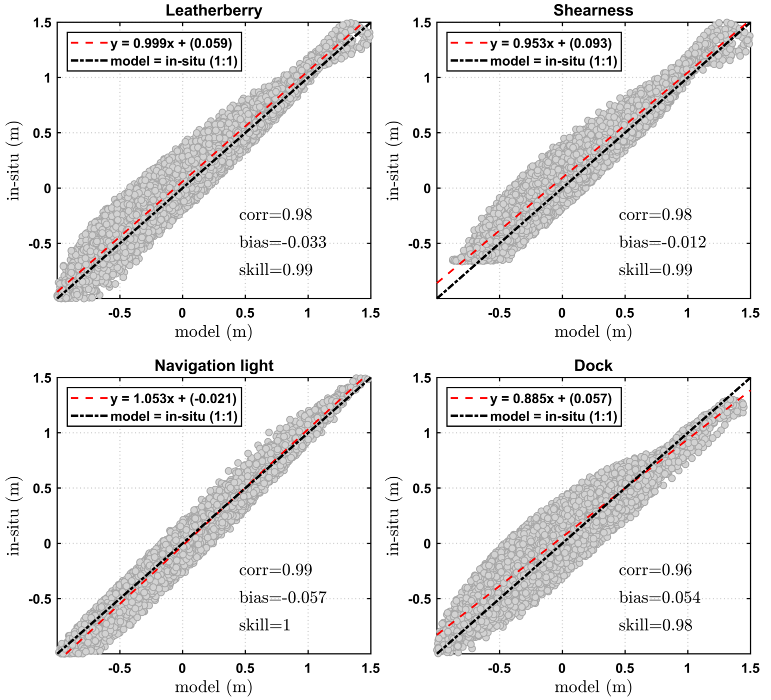

FIGURE 6 Scatter comparison (correlation, average bias index and skill) between FVCOM model and in-situ water surface elevation for the year 2015 at different DNREC tide gauges (in meters, from NAVD88 vertical reference level).

3.1.3 | Model validation

The model performance has been evaluated at point locations for a time frame from April to October 2015 and during two extreme events, in terms of water surface elevation in open water, marsh interior channels and on marsh flats. Also, we compared current velocity during April-May 2015 when two 600-KHz Acoustic Doppler Current Profiler (ADCP) were deployed in two major channels, Leipsic River and Duck Creek. Profilers sampled and stored data at every 6-minute interval. The Delaware Bay tide gauge nearest to BHNWR, at Ship John Shoal, is chosen for model evaluation in Delaware Bay (`https://tidesandcurrents.noaa.gov/waterlevels.html?id=8537121`). Four DNREC tide gauges shown in Figure 2, are used for model evaluation in marsh interior channels. All gauges recorded data for the entire year of 2012 and for a period of 7 months from April to October in 2015 at every 15 minutes. Two ADCP gauges were deployed in Leipsic River and Duck Creek during a short period of time in 2015, therefore the depth averaged current velocity field is compared for that separate time window. Model simulations were performed separately for Hurricane Sandy, and the entire year of 2015 that included Hurricane Joaquin.

Comparison of surface elevation and current data sets at the gauge locations in the BHNWR are shown in Figures 6 and 7 where generally a good agreement between the model and in-situ data is obtained. Comparison with initial simulations with biased sub-tidal signals indicates that such correction being used in the forcing data could enhance model performance. First, we have compared model results with the entire 2015 in-situ data set to evaluate overall performance during a period that has both regular (tidal) and stormy (subtidal) conditions (Figure 6). The average bias index and model skill were computed using Equation 3.1 and 3.2 given as

$$Bias = \frac{\sum_{n=1}^{N}(M_n - O_n)}{\sum_{n=1}^{N} O_n} \tag{3.1}$$

$$Skill = 1 - \frac{\sum_{n=1}^{N}(M_n - O_n)^2}{\sum_{n=1}^{N}(|M_n - O| + |O_n - O|)^2} \tag{3.2}$$

Where N is the total number of samples, M_n is the model result, O_n is the observed data and O is the mean of the observed data.

Tide gauge close to the Bay (Navigation Light) is observed to have a higher correlation and skill score of 0.99 and 1.0, respectively, than the other interior gauges. The averaged bias index and slope of the regression line show that the model under-predicts during falling tide. Inside the wetland, scatter seems to increase at Leatherberry and Shearness, where the correlation coefficient and skill reduces to 0.98 and 0.99. Overall, they both show a similar trend where model under-predicts during high tide and then over-predicts at low tide. Moving further to the most upstream gauge (Dock), model accuracy decreases more and now over-predicts during both tidal conditions, prominently during the low tide. The model performance is further assessed for the current velocity variable at two ADCP locations. Figure 2 shows the instrument locations in Duck Creek and Leipsic River, BHNWR. The results shown in Figure 7 indicate that the velocities predicted by FVCOM agree well with the depth-average of observed velocities. Notably, a slight model under-prediction is observed during low water slack at the Leipsic River gauge, and during high water slack at Duck Creek.

After looking into the model performance for the entire 2015, we have looked into the different hurricane conditions to evaluate the bias that is primarily coming from subtidal signals and flawed marsh flooding and draining. More details on model skill at the Bay and channel tide gauge locations, and the over marsh surface is given in the supplemental material section.

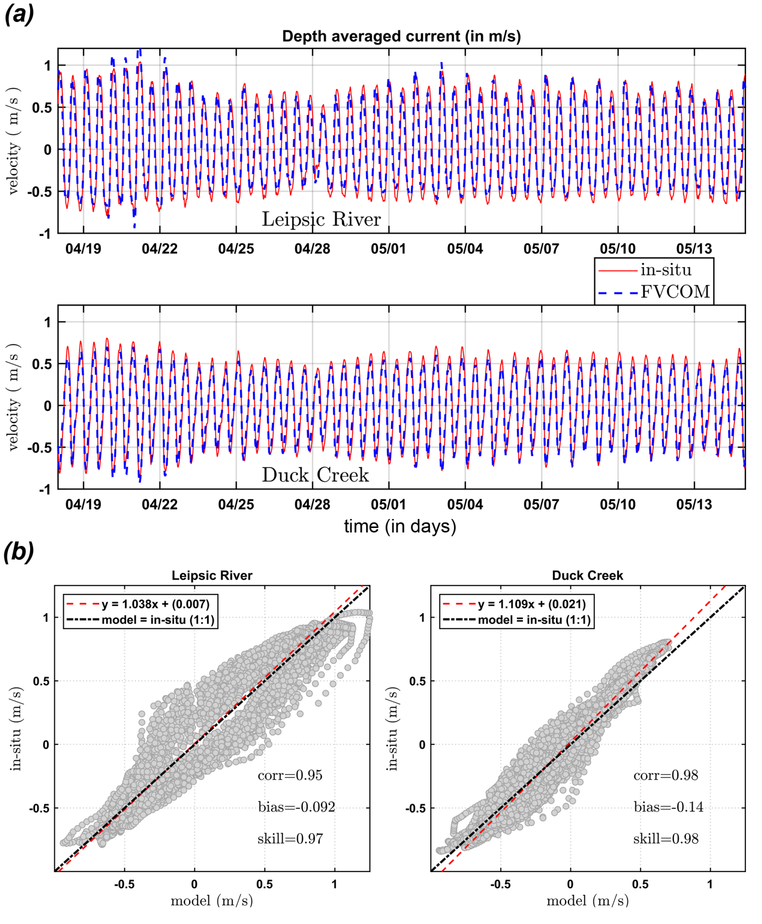

FIGURE 7 (a) Comparison between FVCOM model (in blue) and along-channel depth-averaged current data (in red) collected at different ADCP locations in Bombay Hook during April - May, 2015; (b) Scatter comparison (correlation, average bias index and skill) between FVCOM model and in-situ (in m/s).

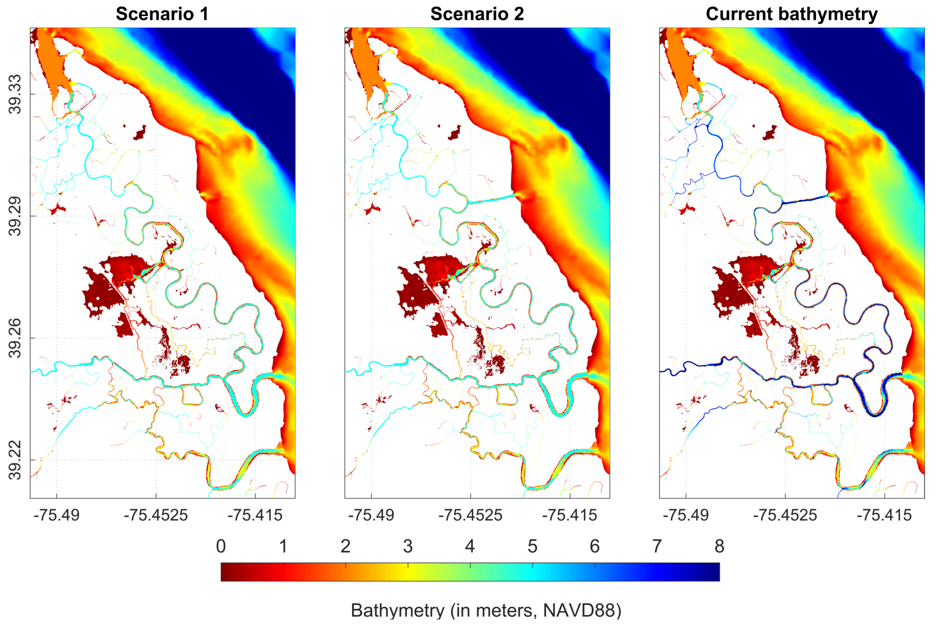

FIGURE 8 Different channel bathymetry conditions (in meters, from NAVD88 vertical reference level). Left subplot: Scenario 1 - No Sluice Ditch and channel depth 5 m, Mid subplot: Scenario 2 - with Sluice Ditch and depth 5 m, Right subplot: Current bathymetry.

3.2 | Quantifying Asymmetry

We have quantified an asymmetry parameter γ_0 following Nidzieko and Ralston (2012) using the time derivative of surface elevation (η_t), mid-channel velocity (U), acceleration of the velocity (U_t), and net flux (Q) from each inlet to represent the duration asymmetry, and velocity and flux skewness for each tidal cycle (using a 12.42 hour window). We selected this relatively simple skewness measure to cope with complex tidal signals and efficiently quantify the variations in tidal surface elevation, current velocity, and volume flux asymmetry over a shorter time scale. Previous studies have quantified the nature and variability of tidal asymmetry using two different methods, mainly: (1) the harmonic method (Aubrey and Speer, 1985; Speer et al., 1991), and (2) the skewness measure (Nidzieko and Ralston, 2012; Guo et al., 2019). The harmonic method can be used as a diagnostic tool to identify the presence and growth of overtides and compound tides from channel bottom friction and geometry (Friedrichs, 2010). The phase differences and amplitude ratios between two or more tidal constituents work as asymmetry indicators where the former represents the direction of asymmetry and later indicates the degree of non-linearity. As the harmonic method is sensitive to the accuracy and length of the time-series data, it cannot resolve all the constituent pairs from records that are too short (Nidzieko and Ralston, 2012). Our field data sets have several critical limitations for validating the tidal constituents generated by the numerical model. The surface elevation data has a couple of missing periods during both the years 2012 and 2015, and we have only a month long ADCP current data which is not sufficient for a reliable harmonic analysis. Besides, in a multi-inlet system, the inlets' geometry can affect the volume flux exchange and generate a tide-induced circulation, making the nonlinearities in velocity more broad-banded (Orescanin et al., 2016). The asymmetry parameter for the velocity, $\gamma_0(U)$ and acceleration, $\gamma_0(U_t)$ are also called the peak current asymmetry and slack water asymmetry, respectively, and previously applied as a proxy for coarse and fine sediment transport estimates (Guo et al., 2018, 2019). More description about the relation between the asymmetry parameters and sediment transport is given in the section 6.2.

Nidzieko and Ralston (2012) calculated second and third moment from the observed time series data sets (surface elevation and velocity) to prescribe the asymmetry parameter as

$$\gamma_0 \equiv \frac{\mu_3}{\mu_2^{3/2}} \tag{3.3}$$

where the k-th moment from zero can be defined as

$$\mu_k = \frac{1}{N-1}\sum_{i=1}^{N}(n_i)^k \tag{3.4}$$

Here, N is the number of samples n_i. When assuming that flood currents are positive, the tide is ebb dominant for $\gamma_0(U) < 0$ and flood dominant for $\gamma_0(U) > 0$ (U is the depth-averaged velocity), and the duration of falling water is longer than rising if $\gamma_0(\eta_t) > 0$. And a positive $\gamma_0(U_t)$ represents a longer high water slack than the low water slack.

4 | CHANNEL BATHYMETRY SCENARIO DEVELOPMENT

As shown in Figure 2a, the BHNWR area is connected to Delaware Bay through four different entrances, including Leipsic River, Simons River, Sluice Ditch/Duck Creek, and Woodland Beach, which are connected via interior channels of the wetland system. Of these, the Sluice Ditch channel is an artificially opened inlet (Dozier, 1947). The ongoing erosion events at the top and mid-portion of the BHNWR, consisting of Leipsic River, Sluice Ditch, and Woodland Beach, have led to examine a few channel morphology scenarios. As there are no land elevation data sets or references available to mimic the historical marsh conditions during the artificial inlet construction, we considered only assigning channel bathymetry that could have been in place at that time. First, we hypothesized a case assuming channel bathymetry set to a maximum depth of 5 m throughout the entire wetland system and artificially filled the existing Sluice Ditch (Figure 8, left). The maximum channel depth is taken based on a few historical reports mentioned in section 2. Also, we observed it be similar to the current Simons River cross-section averaged bathymetry of the undisturbed region. Then, we considered a similar case of channel depth limited to 5 m but introduced Sluice Ditch back into the system (Figure 8, middle). This scenario illustrates the role of an artificially opened inlet like Sluice Ditch in altering the hydrodynamics and enhancing transport processes in a connected system. Ultimately, both of them are compared to the baseline condition with current irregular channel bathymetry where mid-channel depth is close to 10.0 m in Leipsic River and Sluice Ditch (Figure 8, right). The first scenario is a step toward simulating a channel bathymetry condition possibly in effect before the significant marsh erosion. We made no corresponding attempt to narrow channels or recreate river oxbows that have been straightened. We also note that the tidal flat areas such as Money Marsh would have been areas of continuous marsh platform, further reducing the available volume for tidal exchange. Ultimately, we carried out model simulations using these simple channel morphology scenarios to address the following issues:

1. The present condition of the wetland interior and inlet tidal asymmetry (flood/ebb dominance) and mean circulation.
2. The wetland tidal range, flow asymmetry, and frictional regime's response to a reduced channel depth and closure

of the artificially opened inlet.

3. The changes to the tidal dynamics and mean circulation from progressive channel deepening since the inlet construction.

They are explored in section 5 and discussed in section 6 to relate the changes in channel tidal dynamics to the wetland's overall erosive trend.

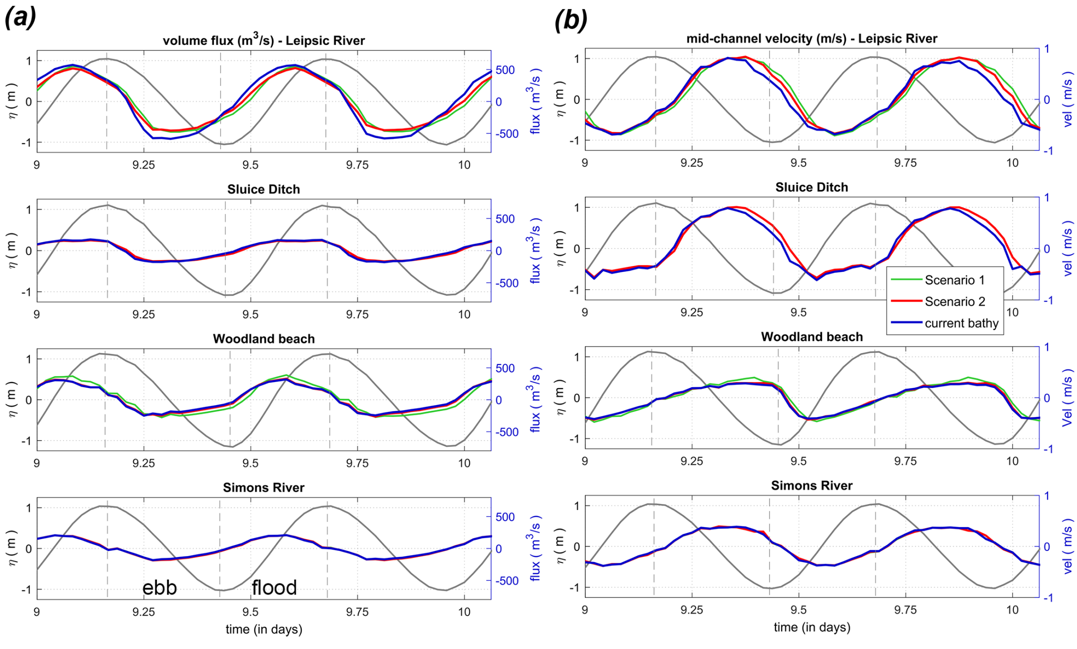

FIGURE 9 Volume flux (in m^3/s) going in/out through BHNWR inlets and the respective mid-channel velocities. First subplot (a) shows flux magnitude during a spring cycle for different inlets. The color lines represent flow conditions based on different morphology scenarios (Green: Scenario 1 - No Sluice Ditch and depth 5 m, Red: Scenario 2 - with Sluice Ditch and depth 5 m, Blue: Current bathymetry). Second subplot (b) represent the mid-channel velocity for the same inlets. Surface elevation from respective inlet entrance location (referenced to NAVD88, in meters) is shown with the solid gray line.

5 | RESULTS

For the scenario analysis, we selected M_2, the major tidal constituent in the Delaware estuary (Parker, 1984) and the principal solar semidiurnal constituent S_2 for open boundary forcing to evaluate the simple effect of the wetland morphology on tidal volume exchange and the respective flood/ebb dominance of the system during spring-neap cycles. A month-long simulation covering the entire spring-neap process is done using the tidal amplitude and phase information taken from the nearest NOAA tide gauge. All model parameters were kept the same as described earlier in section 3.1.2. The inlets can show cross-channel spatial asymmetry, therefore, the total volume flux going in and out of the system is calculated across each inlet, along with the mid-channel velocity to show the nature of hydrodynamics at the deeper part. Figure 9 show the total flux going in/out through BHNWR inlets and velocity magnitudes separated for a spring cycle. Multiplying depth-averaged velocity with time-varying total depth ($h+\eta$) and width provides volume flux through each cell face at the transect, and an integral over the transect represents total volume flux at each inlet. We have used the same linear function described in FVCOM manual (Chen et al., 2013) for velocity reconstruction at the cell faces. The tidal amplitude and phase at different inlet locations have a synchronous response, and they are almost identical for all the scenarios. So, we chose the Leipsic river inlet surface elevation from current bathymetry for the comparison shown in Figure 9. The model results from different scenarios are described in the following subsections.

5.1 | Flood/ebb dominance of the system based on current bathymetry

From Table 1-2, we can see that all the river inlets are observed to have a positive duration asymmetry and represent a longer falling tide than rising. However, interestingly, the Leipsic River and Sluice Ditch inlets are observed to be ebb dominant, with higher velocities during ebb tide than flood tide and a $\gamma_0(U) < 0.0$, while Woodland Beach and Simons River are flood dominant. It is apparent that the ebb tidal flux also shows ebb dominance in Leipsic River and Sluice Ditch for the present marsh and spring tide conditions. To look into the primary causes responsible for the inlet asymmetry, we evaluated the net tide-induced residual for each tide cycle at all the inlet entrances, shown in Figure 10b. From the residual balance, we can see that the net flow goes in through the Woodland Beach inlet and then leaves via Leipsic River and Simons River inlets. This residual flux is close to 1% of the total volume that goes in/out of the entire wetland shown in Figure 10a. Interestingly, the overall circulation is observed to play a critical role in the asymmetry calculations. In Table 1-2, we have added two more asymmetry parameters $\gamma_0(U_{mr})$ and $\gamma_0(Q_{mr})$ that represent mean removed velocity and flux skewness during both spring and neap tide. In absence of the tide-induced residual, the Leipsic River and Sluice Ditch inlets show less ebb dominance, where Woodland Beach shows less flood dominance at the same spring cycle. The asymmetry pattern at the interior gauges follows a similar trend of Leipsic River and Sluice Ditch inlets, where Dock is located toward the upstream end of Leipsic River, and Leatherberry gauge sits close to Sluice Ditch inlet.

In tidal channels, beside the system's tidal circulation, the bathymetry induced across-channel flow variation and small channel vortices can also contribute to the local velocity skewness (Becherer et al., 2015). In Table 1-2, we can observe the effect of these complex local processes in the inlet flux asymmetry, where the magnitude of the mean removed velocity and flux skewness is still large at some locations. Now, as the connected tidal channels have rapidly varying bathymetry in both lateral and longitudinal directions, it is incredibly challenging to identify the other major sources of asymmetry for the entire system. Changes to the channel bottom slope, time-varying water depth, channel cross-section area, and bottom friction can alter the velocity skewness from place to place, ultimately affecting the flux skewness. To illustrate this non-linear interaction, we have selected a channel transect in the Simons River inlet, shown in Figure 11, and compared the momentum balance terms following Huang et al. (2008). More details on the FVCOM 2D momentum equations are given in section 8. The Simons River inlet has a relatively minor contribution to the system's net circulation during spring tide, and the flux asymmetry given in table 1 is from the local flow and channel properties. The three circles are shown in Figure 11a represent three different portions of the channel, from the shallower side bank to the deeper portion, and display the terms from the model depth-integrated U-momentum equation. Terms from the model V-momentum equation are comparatively smaller in magnitude and neglected for this analysis. Then, we picked only the major contributors: the advective inertia (ADV), barotropic pressure gradient (DP), bottom friction (FRIC) and the horizontal viscosity (Diff) from equation 8.1 for the balance comparison. In Figure 11b, we can see that, during a rising tide, at the transition zone (i.e., location representing sharp across-channel bathymetry change), the advection term is much larger compared to the other two portions and balanced by the bottom friction and pressure gradient. In the shallower and deeper portion, even though the terms in the momentum equation are much smaller, we can observe that the pressure gradient balances the advective inertia and bottom friction in the shallow side bank. In contrast, the channel mid-portion and deeper side show the dominant balances between the pressure gradient and the advective inertia during ebb. The lagged discharge due to reduced channel cross-section area comes out through the narrow and deeper portion of the channel, showing an ebb dominance for that part. Ultimately, this assessment illustrates the across-channel variation in the momentum terms from inlet and channel geometry that contribute to the across-channel velocity skewness. A similar dynamic could also be in place at the Woodland Beach inlet, where we still see a flood dominant velocity and flux asymmetry in the table 1 even when the mean is removed.

5.2 | Effect of an artificially opened inlet channel

For the first scenario, all the inlets are observed to be flood dominant based on the duration asymmetry. This can be evident from (Table 1-2), where we can see that $\gamma_0(\eta_t) > 0$ everywhere. The reduced thalweg depth and channel geometry have reduced the volume flux through the Leipsic River, and the inlet shows a flood dominant condition where $\gamma_0(Q) > 0$ in Table 1). Woodland Beach and Simons River, the remaining inlets, also show flood dominance based on the volume flux skewness. As indicated earlier, the flow dynamics at all the inlet entrances have a complex contribution from the net circulation and the local bathymetry-induced effects. When looking at the velocity, this was evident as the Leipsic River and Simons River inlets display asymmetrical across-channel flow, where the deeper portion is ebb dominant and $\gamma_0(U) < 0$. The interior channel gauges show similar characteristics to the inlet thalwegs. While the Dock gauge on Leipsic River is ebb dominant, the Leatherberry gauge, not connected to Sluice Ditch for this scenario, shows flood dominance similar to the Woodland Beach inlet (Table 1)). Then, we have estimated the mean residual at the inlet entrances to evaluate the role of tide-induced circulation in the overall asymmetry variation. From Figure 10b, we can see that the major two inlets, Leipsic River and Woodland beach inlet, have a net balance in the absence of Sluice Ditch, where there is a landward mean flux at Woodland beach inlet and seaward at the other. While the residual flux is even less than 1% of the total volume, it still plays an essential role in the asymmetry calculation. If we take the mean flux out of asymmetry calculation, the ebb dominant inlet thalwegs immediately show flood dominance where $\gamma_0(U_{mr})$ are positive numbers. Now, compared to the peak current asymmetry $\gamma_0(U)$, the slack water asymmetry $\gamma_0(U_t)$ is observed to be flood dominant at the inlet and interior gauges. During the neap cycles, we can see a similar trend in asymmetry, shown in Table 2. Overall, the entire system has a flood dominant condition based on the volume flux skewness, duration asymmetry, and slack water asymmetry for this scenario.

When Sluice Ditch is introduced into the bathymetry of the first scenario (with the limitation to 5m depth), the total instantaneous flux going in or out of the Leipsic River becomes more asymmetric during both spring and neap conditions (Table 1-2). The introduction of Sluice Ditch has increased Leipsic River inlet volume flux ebb dominance, along with the interior connecting channel's velocity ebb skewness shown in Figure 12. The tide averaged circulation now shows a balance between the flood dominant Woodland Beach inlet and ebb dominant Leipsic River and Sluice Ditch inlets during spring tide. Interestingly, during neap, we see that the Simons River inlet also contributes to the net volume flux balance and shows an increased ebb dominance. Again, the circulation effect is observed to an important factor in the asymmetry calculation as the flux and velocity skewness $\gamma_0(U_{mr})$ and $\gamma_0(Q_{mr})$ in Table 1-2 becomes close to zero at ebb dominant inlets and the marsh interior. The Woodland Beach inlet remained flood dominant with an increase in thalweg flood velocity asymmetry. In addition, the slack water asymmetry at the interior gauge Leatherberry has flipped and immediately became ebb dominant from the introduction of Sluice Ditch. Based on the results, we can state that, while this artificially constructed channel itself is ebb dominant, it has also impacted two other locations significantly: the Leipsic River entrance and the interior connecting channel Duck Creek. The flow at those entrances and the interior channel show strong ebb dominance, favoring a seaward export.

The opening of Sluice Ditch also has a pronounced effect on the tidal range in all areas of the system aside from those most adjacent to the Leipsic and Woodland Beach entrances, with the tide range doubled in some instances along Duck Creek and at the entrance into Money Marsh, shown in Figure 13a. The increase in tide range is specifically coming from the rise in mean low water along the Duck Creek (Figure 14a, Leatherberry), even without the effect of depth change. The opening reduces the maximum velocity in some instances along Leipsic River and Duck Creek up to the entrance of the Money Marsh mudflat area; however, it caused a dramatic increase in the maximum velocity from there to the vicinity of the inlet (Figure 13c). From the Leatherberry mid-channel velocity shown in Figure 14b, we can see that the velocity magnitude skewness has increased and became more ebb dominant with the opening of Sluice Ditch. The subsequent impact on the system's frictional regime, net sediment transport, and marsh erosion is discussed in section 6.

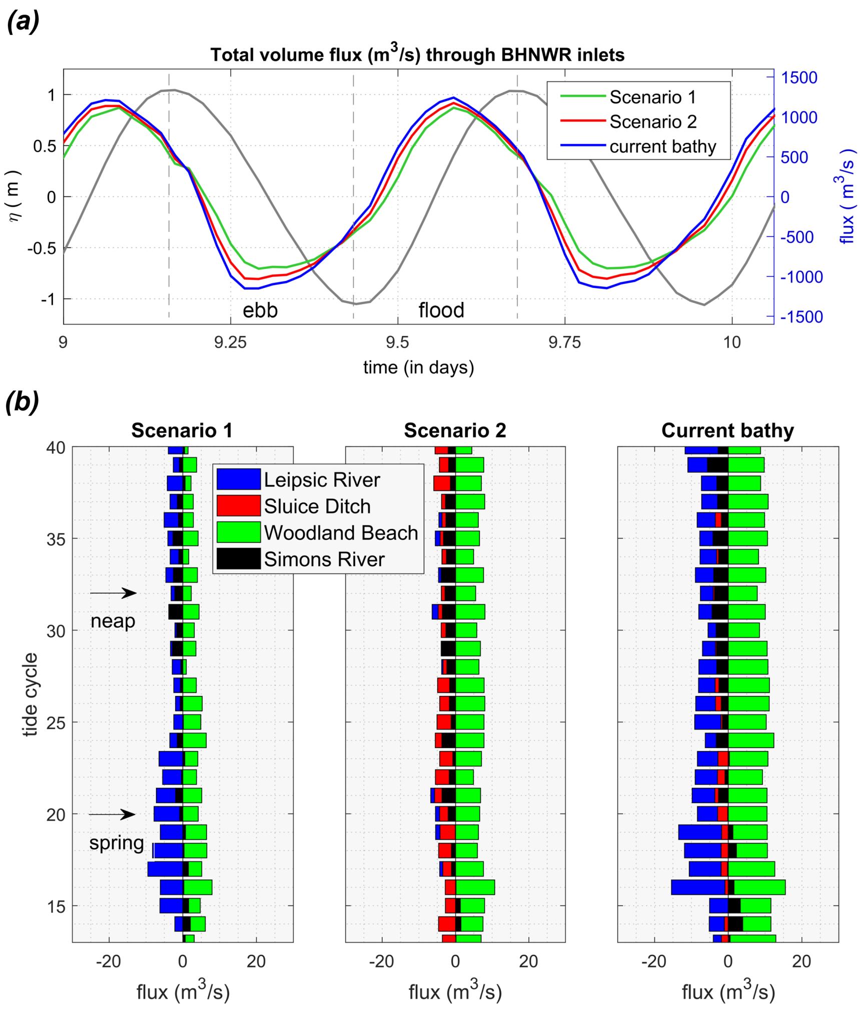

FIGURE 10 (a) Total volume flux (in m^3/s) going in/out of the entire BHNWR wetland during a spring tide for different morphology scenarios (here, positive flux represents going into the wetland, negative represents going out); (b) Tide-averaged volume flux residual at major inlet locations for different morphology scenarios.

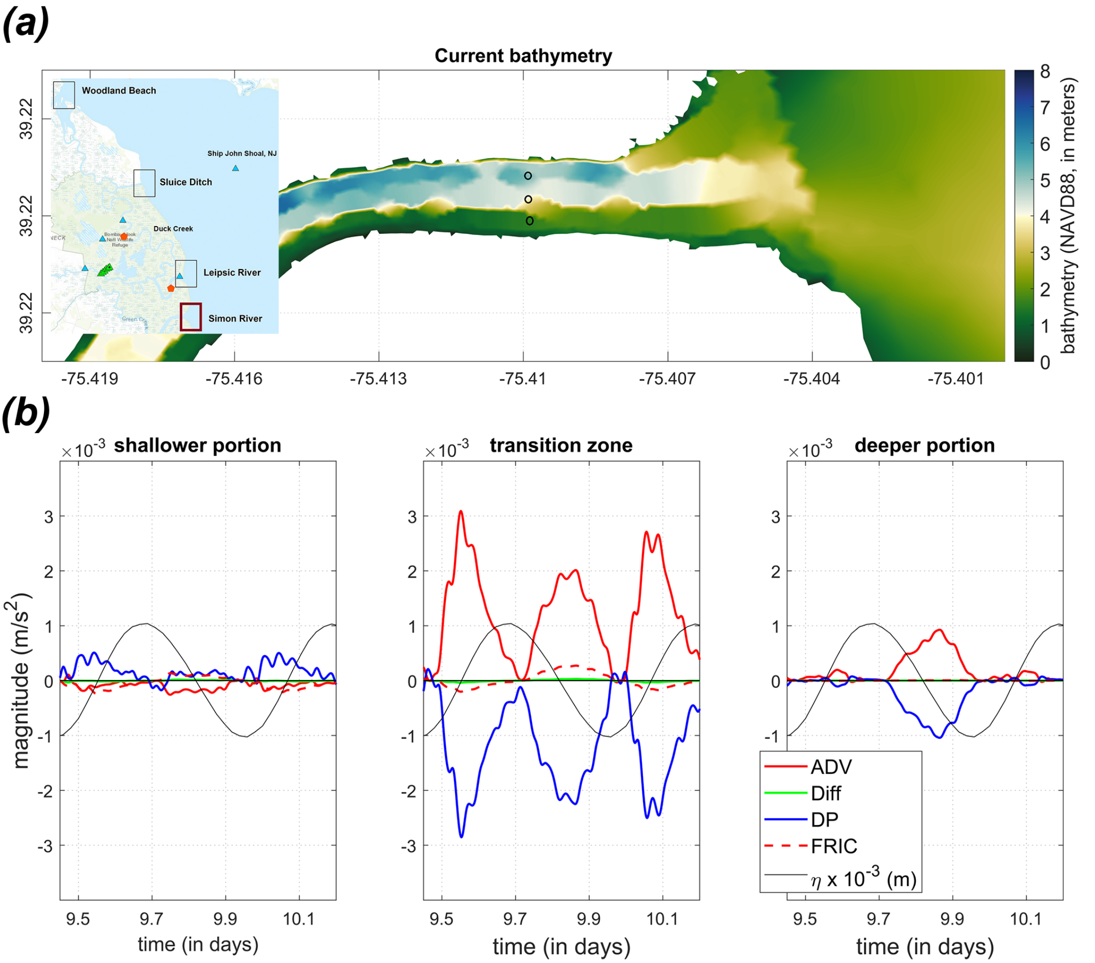

FIGURE 11 (a) The Simons River inlet present bathymetry (in meters, from NAVD88 vertical reference level) and the three black circles represent the locations used for the momentum balance analysis; (b) Momentum terms: the advective inertia (ADV), barotropic pressure gradient (DP), bottom friction (FRIC) and the horizontal viscosity (Diff) from model depth-integrated U-momentum equation during a spring tide cycle. Surface elevation from inlet entrance is shown with the solid gray line.

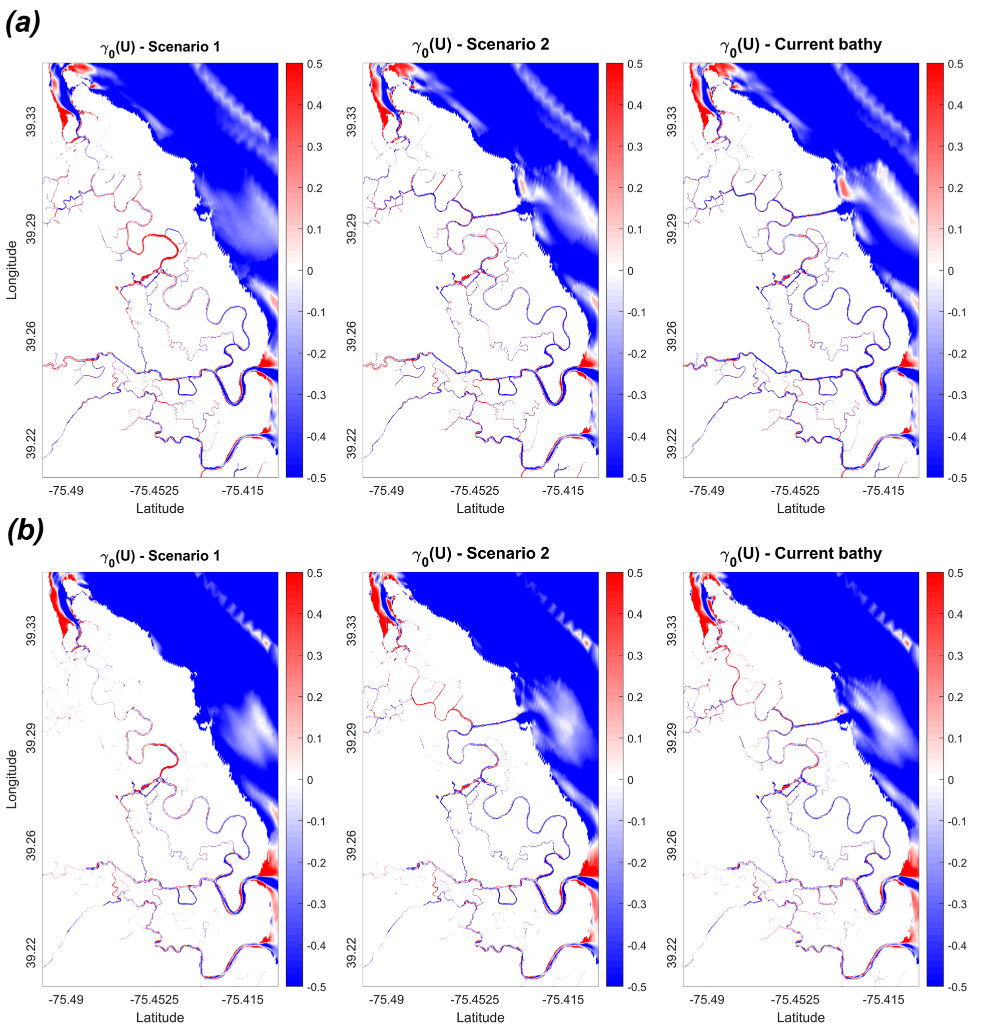

FIGURE 12 Spatial changes in velocity skewness/peak current asymmetry $\gamma_0(U)$ for different morphology scenarios (a) during a spring tide cycle; (b) during a neap tide cycle. Here, positive and negative values show flood and ebb dominant asymmetry respectively.

5.3 | Effect of progressive channel deepening

Comparing the present-day conditions (i.e., Current bathy (CB)) with second scenario, we can see that the volume flux is more asymmetric and ebb dominant at the Leipsic River inlet, even though the velocity skewness at the thalweg reduces (Table 1). Woodland Beach, a flood dominant inlet in the case of both the first and second scenario, shows an increased flood dominance. Among other gauges, the interior gauge at Leatherberry exhibits the most changes in velocity skewness $\gamma_0(U)$ where the ebb asymmetry almost doubled during spring tide. This phenomenon has another important implication: the interior connecting channel's ebb skewness increased from the progressive channel deepening, leading to a more erosive condition in the marsh interior. The tide-induced circulation estimate shows that the residual magnitude has increased, where the balance is primarily between the Woodland Beach inlet and the Leipsic River inlet (Figure 10). During neap tide, there is an increase in residual magnitude at the Simons River inlet. The mean removed asymmetry indicates that the Leipsic River inlet and Leatherberry gauge have increased ebb dominance from channel property changes (i.e., bathymetry, cross-section area), even if we do not take the net circulation into account. The slack water asymmetry $\gamma_0(U_t)$, a proxy for the fine sediment transport, shows an increased ebb asymmetry at the Leipsic River and Sluice Ditch inlets and the marsh interior gauges. Other processes such as the tide range have increased to some extent from mean low water increase, at the upstream side of Leipsic River and the interior gauge Leatherberry, shown in Figure 13b and 14a. At the same time, the maximum velocity change is observed to have a spatially varying response (Figure 13d). It provides an important insight into the effect of spatially varying channel cross-section area and the net circulation in changing the wetland's interior and inlet hydrodynamics. Ultimately, we can see that the increase in channel bathymetry over time has made some areas of the wetland system more ebb dominant, which can contribute to the ongoing erosion. Further details on the relation between the asymmetry changes and the net sediment transport is given in section 6.

TABLE 1 Asymmetry parameters calculated at the channel inlet and marsh interior tide gauge locations during a spring tide cycle

Inlets	Leipsic River			Sluice Ditch			WB			Simons River		
	Scn 1	Scn 2	CB	Scn 1	Scn 2	CB	Scn 1	Scn 2	CB	Scn 1	Scn 2	CB
$\gamma_0(U)$	-0.44	-0.48	-0.24		-0.78	-0.61	0.17	0.43	0.48	-0.18	-0.21	-0.25
$\gamma_0(U_{mr})$	0.05	-0.01	-0.03		-0.13	-0.12	0.26	0.36	0.35	0.06	0.07	0.07
$\gamma_0(Q)$	0.07	-0.05	-0.11		-0.09	-0.06	0.39	0.36	0.42	0.17	0.14	0.21
$\gamma_0(Q_{mr})$	0.12	0.09	-0.03		0.03	-0.01	0.31	0.23	0.16	0.17	0.17	0.21
$\gamma_0(U_t)$	1.31	0.96	-0.28		-0.19	-0.55	1.30	1.42	1.46	0.34	0.37	0.37
$\gamma_0(\eta_t)$	0.21	0.22	0.23		0.29	0.29	0.41	0.41	0.43	0.21	0.22	0.22
Interior	**Leatherberry**			**Dock**								
	Scn 1	Scn 2	CB	Scn 1	Scn 2	CB						
$\gamma_0(U)$	0.14	-0.23	-0.44	-0.23	-0.29	-0.26						
$\gamma_0(U_{mr})$	0.26	0	-0.1	0.12	0.10	-0.04						
$\gamma_0(U_t)$	0.11	-0.40	-0.44	0.07	-0.07	-0.48						
$\gamma_0(\eta_t)$	0.23	0.10	-0.03	0.48	0.46	0.33						

TABLE 2 Asymmetry parameters calculated at the channel inlet and marsh interior tide gauge locations during a neap tide cycle

Inlets	Leipsic River			Sluice Ditch			WB			Simons River		
	Scn 1	Scn 2	CB	Scn 1	Scn 2	CB	Scn 1	Scn 2	CB	Scn 1	Scn 2	CB
$\gamma_0(U)$	-0.34	-0.33	-0.02		-0.67	-0.51	0.23	0.55	0.59	-0.16	-0.19	-0.24
$\gamma_0(U_{mr})$	0.01	-0.01	-0.02		-0.18	-0.16	0.29	0.34	0.36	0.06	0.06	0.08
$\gamma_0(Q)$	0.05	0.01	-0.07		-0.16	-0.15	0.30	0.38	0.48	0.03	-0.01	0.03
$\gamma_0(Q_{mr})$	0.08	0.05	-0.01		-0.04	-0.05	0.25	0.25	0.26	0.08	0.08	0.12
$\gamma_0(U_t)$	1.21	1.01	-0.01		0.04	-0.24	1.66	1.18	1.01	0.34	0.29	0.33
$\gamma_0(\eta_t)$	0.16	0.16	0.17		0.20	0.19	0.31	0.30	0.29	0.16	0.15	0.16

Interior	Leatherberry			Dock		
	Scn 1	Scn 2	CB	Scn 1	Scn 2	CB
$\gamma_0(U)$	0.01	-0.36	-0.44	-0.18	-0.19	-0.07
$\gamma_0(U_{mr})$	0.16	-0.12	-0.16	0.12	0.09	0.04
$\gamma_0(U_t)$	0.18	-0.41	-0.54	0.54	0.49	0.39
$\gamma_0(\eta_t)$	0.15	-0.01	-0.08	0.34	0.32	0.22

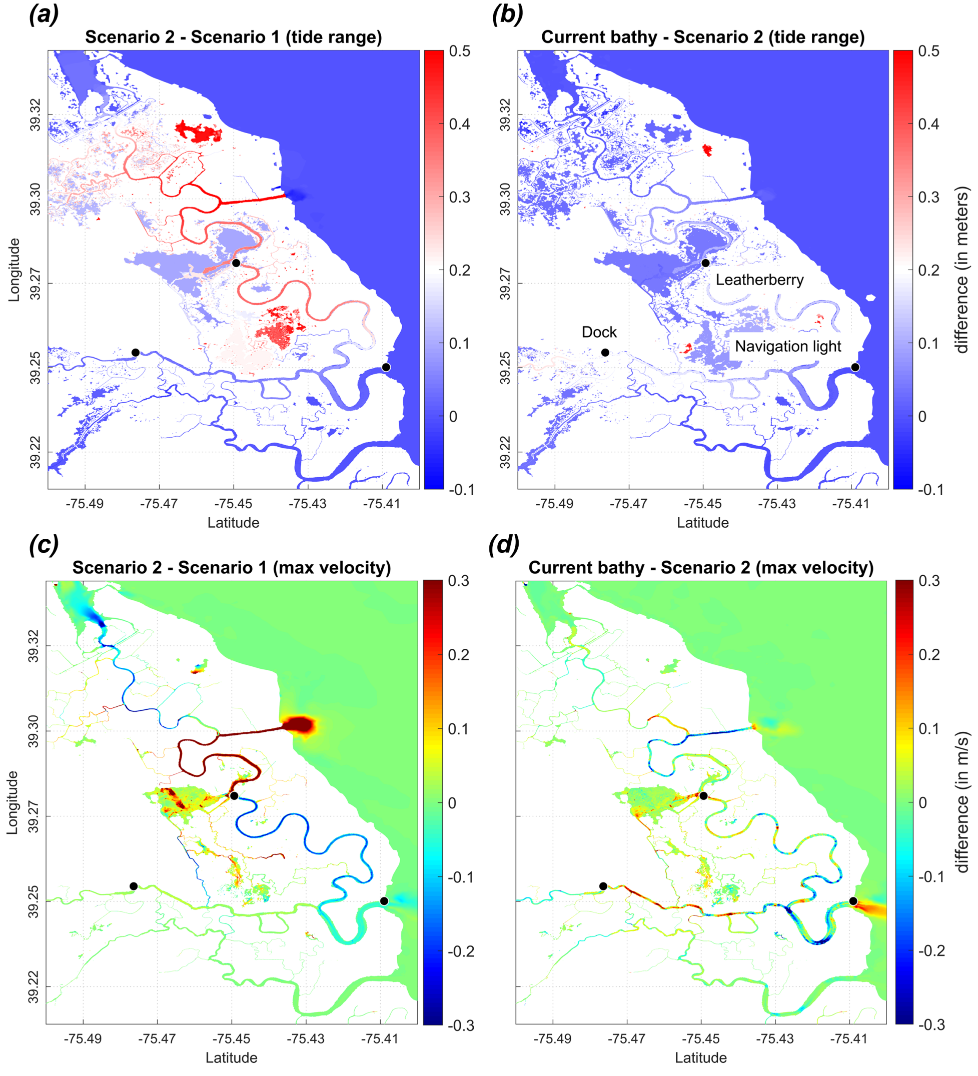

FIGURE 13 (a) Changes to the tide range from artificial dredging of Sluice Ditch (in meters). The tide range estimated from Scenario 1 (No Sluice Ditch and depth 5 m) is subtracted from the tide range of Scenario 2 (with Sluice Ditch and depth 5 m); (b) Similar subtraction is done between Scenario 2 and current bathymetry (in meters); (c) Changes to the maximum velocity from artificial dredging of Sluice Ditch (in m/s). Here, the maximum velocity magnitude for the case of Scenario 1 (No Sluice Ditch and depth 5 m) is subtracted from the maximum velocity magnitude of Scenario 2 (with Sluice Ditch and depth 5 m); (d) Similar subtraction is done between Scenario 2 and current bathymetry (in m/s).

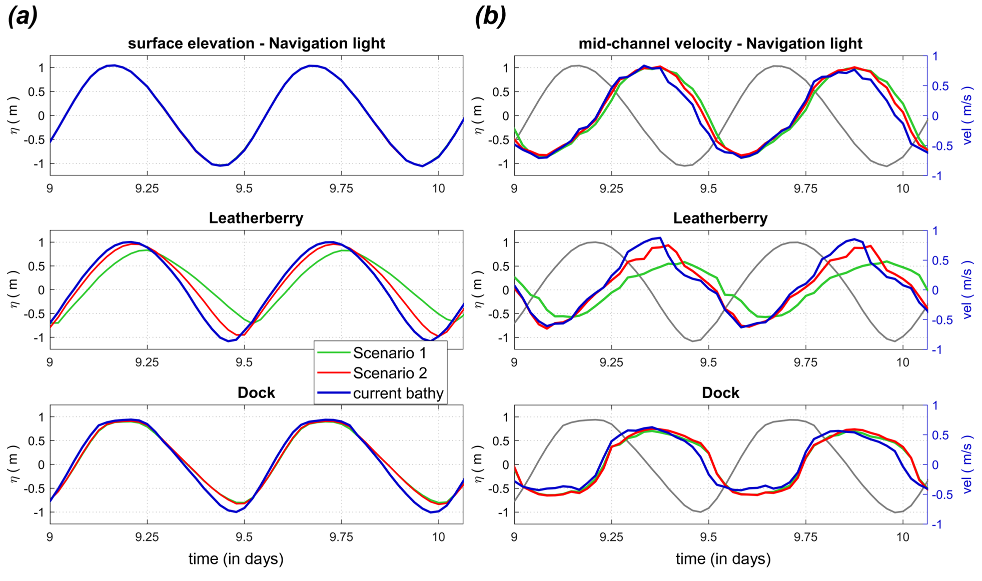

FIGURE 14 (a) Model surface elevation for different morphology scenarios at interior tide gauge locations during a spring cycle (in meters, from NAVD88 vertical reference level). Green: Scenario 1 - No Sluice Ditch and depth 5 m, Red: Scenario 2 - with Sluice Ditch and depth 5 m, Blue: Current bathymetry; (b) Mid-channel velocity for different morphology scenarios at the same gauges (in m/s). Surface elevation for current bathymetry scenario (referenced to NAVD88, in meters) is shown with the solid gray line to represent the flood and ebb tide.

6 | DISCUSSION

6.1 | Loss of frictional dominance

In the previous section, we noticed that the inlet and channel morphology changes had altered the volume flux and the net tide-induced residual going in/out of the system. Figure 13 and 14 show that the shift in volume flux balance can affect the marsh interior tide range and reduce the frictional dominance. To understand these changes in the system's interior from the artificial opening in a mechanistic way, we have also used a simple ocean-inlet-bay model that connects the wetland interior to the offshore by separate inlets. The Money marsh mudflat (where Leatherberry tide gauge is located) acts like a small Bay system which in reality is connected to the Delaware Bay by two separate major inlet channels, both in the first and second scenario. The major difference between both scenarios can be understood from Figure 15a. We can see the dramatic change in the ocean-inlet-bay system after introducing the new channel, where the interior now has a much shorter connection and higher depth for the tidal exchange compared to the first scenario. Here, we use the ocean-inlet-bay analytical model proposed by Aretxabaleta et al. (2017) to evaluate the first-order response of the bay to ocean sea level forcing. Aretxabaleta et al. (2017) studied a similar shallow estuarine system in southern Long Island, New York along the Atlantic Ocean, and developed the bay water level expression (Equation 6.3) using along-channel depth-averaged momentum equation. Based on the simple balance between local inertia, frictional effects and pressure gradient, the momentum and continuity equations can be written as

$$\frac{\partial u_n}{\partial t} = g\frac{(\eta_o - \eta_e)}{L_n} - \frac{r_n}{h_n}u_n \tag{6.1}$$

$$A_e\frac{\partial \eta_e}{\partial t} = \sum h_n W_n u_n \tag{6.2}$$

where A_e and η_e are the surface area and sea level in the bay; η_o the sea level in the ocean; with h_n the water depth; u_n the depth-averaged velocity; W_n the width and L_n the length of channel n, and r is the linear drag coefficient ($\approx \frac{8}{3\pi}u$), for $n = 1, 2$.

Assuming $\eta = \eta e^{i\omega t}$ and $u = u e^{i\omega t}$ gives the result

$$\eta_e = \eta_o\left\{\frac{\frac{h_1 W_1 g}{L_1\left(\frac{r_1}{h_1}+i\omega\right)} + \frac{h_2 W_2 g}{L_2\left(\frac{r_2}{h_2}+i\omega\right)}}{i\omega A_e + \frac{h_1 W_1 g}{L_1\left(\frac{r_1}{h_1}+i\omega\right)} + \frac{h_2 W_2 g}{L_2\left(\frac{r_2}{h_2}+i\omega\right)}}\right\} \tag{6.3}$$

where ω is the radian frequency of the ocean tidal oscillation and $\frac{r_n}{h_n}$ is the characteristics frequency of frictional dissipation in the channel. From the denominator in the Equation 6.3, we can also estimate the undamped natural frequency w_n of the interior bay (Helmholtz frequency) as

$$w_n = \left(\frac{h_1 W_1 g L_2 + h_2 W_2 g L_1}{A_e L_1 L_2}\right)^{1/2} \tag{6.4}$$

As the characteristic frequency of channel frictional dissipation increases from lower depth and higher friction, it reduces the frictional adjustment time and increases the interior amplitude damping. According to Chuang and Swenson (1981), when $\frac{r_n/h_n}{w_n} > 1.0$, the range of water level variation inside the bay is always less than the ocean, and for a

TABLE 3 Channel-Bay properties inside BHNWR

Variables	W1	h1	L1	W2	h2	L2	w_n	$\frac{r_n/h_n}{w_n}$
Scenario 1	100.0 m	5.0 m	17 km	200.0 m	2.0 m	19 km	3.96×10^{-4}	5.4
Scenario 2	100.0 m	5.0 m	17 km	100.0 m	5.0 m	10 km	4.96×10^{-4}	2.4
Current bathy	100.0 m	8.0 m	17 km	100.0 m	10.0 m	10 km	6.75×10^{-4}	1.0
Tidal period, T	12.42 hours							
Money marsh mudflat area, A_e	1.0×10^6 m^2							
Drag coefficient, r_n	3.0×10^{-3}							

$\frac{r_n/h_n}{w_n} \leq 1.0$ the response is opposite.

Based on the ocean-inlet-bay properties in our first and second scenario and ocean surface elevation from the FVCOM model, we have estimated the changes in channel frictional dissipation, natural frequency of the system and the decay time (Table 3). The analytical model result is shown in Figure 15b for different morphology scenarios, and we can see that the amplitude response η_e in the bay (marsh mudflat) mimic results seen from the numerical model in Figure 14a (Leatherberry gauge). To check the primary role of the inlet length and depth only, we kept the linear drag coefficient equal to 3.0×10^{-3} that normally varies based on the channel depth. The ratio of amplitude decay time $\frac{r_n}{h_n}$ and undamped natural frequency w_n is observed to be 5.4 for the first scenario due to the shallow ($h_2 \sim 2.0m$) and long ($L_2 \sim 19km$) inlet channel going toward the Woodland Beach. After adding the man-made channel Sluice Ditch, we can see that the shorter and deeper side ($h_2 \sim 5.0m$ and $L_2 \sim 10km$) has reduced the characteristics frequency of channel frictional dissipation, increased the natural frequency, and ultimately reduced the ratio to 2.4. From the surface elevation comparison in Figure 15b, we can see a bigger tidal range and reduced bay amplitude damping compared to the first scenario, also shown in FVCOM results (Figure 14a).

At the marsh interior tide gauges, Leatherberry and Dock (Figure 14a), we can see that the tide range has increased along the channel compared to the shallower bathymetry, and the increase again is coming from the asymmetric response where the mean low water increased more compared to the decrease in mean high water. Familkhalili and Talke (2016) and Ralston et al. (2019) have observed a similar scenario in Cape Fear River Estuary, NC and Hudson River Estuary respectively, where the channel deepening by dredging has increased the tidal range by decreasing the effective drag and increasing hydraulic conveyance.

If we compare scenario 2 and the current bathymetry, it is not trivial to explain all the observed changes at different locations using simple analytical models because of the internal connection between the three inlets. We chose a short stretch from the Leipsic River and Duck Creek junction to the Leipsic River upstream tide gauge (can be considered a straight river reach) to demonstrate the effect of bathymetry change on the frictional regime. For a channelized tidal estuary, Friedrichs and Madsen (1992) express the cross-sectionally averaged momentum equation as

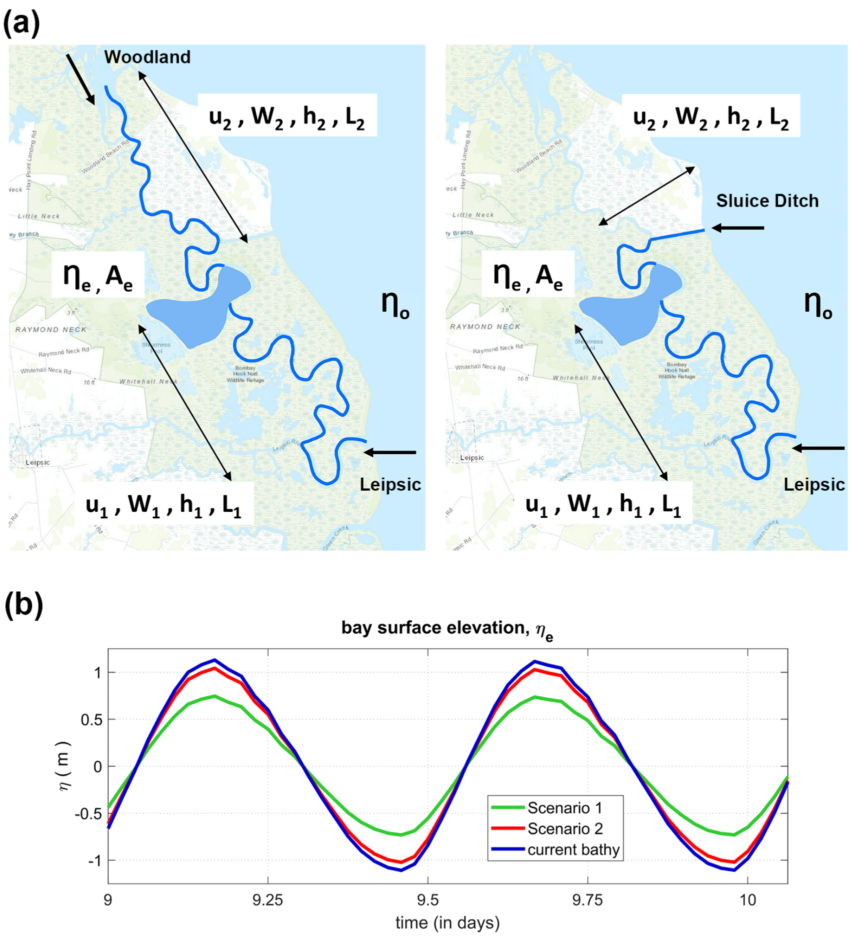

FIGURE 15 (a) Diagram of the ocean-inlet-bay system inside BHNWR; left subplot: Scenario 1 - No Sluice Ditch, and the interior is connected via Leipsic River and the Woodland beach inlet; right subplot: Scenario 2 and current bathymetry - after introducing Sluice Ditch; (b) Surface elevation, η_e for different morphology scenarios at the Money Marsh mudflat using the analytical model (in meters, from NAVD88 vertical reference level).

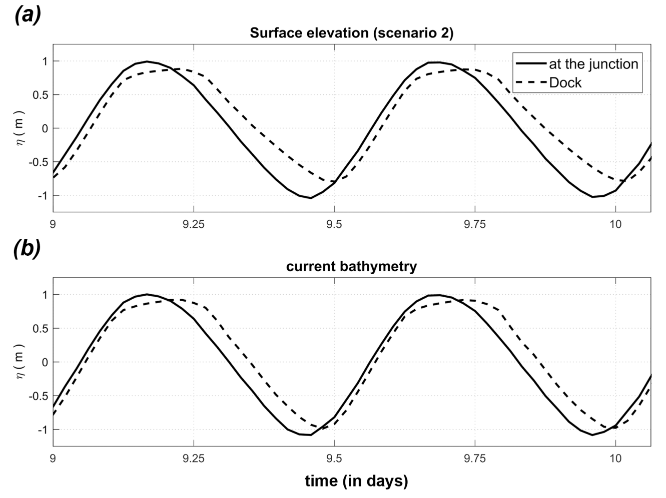

FIGURE 16 Changes in surface elevation from channel deepening along a short stretch in Leipsic River (referenced to NAVD88, in meters).

$$\frac{\partial u}{\partial t} + u\frac{\partial u}{\partial x} + g\frac{\partial \eta}{\partial x} + \frac{C_d u|u|}{\eta + h} = 0 \tag{6.5}$$

where, h is the cross-sectionally averaged depth of channel; η is the surface elevation; u is the cross-sectional average velocity; and C_d is the drag coefficient. Scaling the tidal amplitude with ξ, velocity with U, time with the tidal period T, x with a characteristic length scale L, characteristic depth scale H, we define non-dimensional variables $x_0 = x/L$, $t_0 = t/T$, $u_0 = u/U$, $h_0 = h/H$, $\eta_0 = \eta/\xi$. In terms of these scaled variables, Equation 6.5 becomes

$$S\frac{\partial u_0}{\partial t_0} + I u_0\frac{\partial u_0}{\partial x_0} + \frac{\partial \eta_0}{\partial x_0} + R\frac{u_0|u_0|}{h_0 + \epsilon\eta_0} = 0 \tag{6.6}$$

The non-dimensional parameters S, I and R are given by

$$S = \frac{1}{\epsilon}\frac{F^2 L}{UT} \tag{6.7}$$

$$I = \frac{F^2}{\epsilon} \tag{6.8}$$

$$R = \frac{F^2 C_d L}{\epsilon H} \tag{6.9}$$

where $\epsilon = \xi/H$ and F is the Froude number $U/\sqrt{gH}$. From our chosen channel reach we have noticed that the tidal amplitude is $0.8m$ and $1.0m$, and cross-sectionally averaged channel depth is $\sim 3.0m$ and $\sim 5.0m$ for the second scenario and the current bathymetry respectively. Using the characteristic scales in the Leipsic River: $L = 16km$, $T \sim 12.42hrs(\sim 45000sec)$, $C_d = 3 \times 10^{-3}$, and $U \sim 0.5m/s$, we have observed that the local inertia S and the advective term I both are in same order. The ratio of tidal amplitude to the mean depth ϵ in all of the above terms (Equation 6.7-6.9) is seen to be two orders of magnitude larger than F^2 for both bathymetry conditions.

From Table 4, we see that friction dominates inertia for both cases where R is an order of magnitude bigger than

TABLE 4 Scales and Parameters for the Leipsic River reach

Bathymetry	U_0 (m/s)	ϵ	F^2	I	S	R
Scenario 2	0.5	0.26	8.5 $\times 10^{-3}$	0.032	0.022	0.512
Current bathy	0.5	0.2	5.0 $\times 10^{-3}$	0.025	0.017	0.24

S and I. For the selected reach of the Leipsic River, the increase in mean low water can be simply explained using a balance between the sea surface gradient and channel friction as

$$g\frac{\partial \eta}{\partial x} + \frac{C_d u|u|}{\eta + h} = 0 \tag{6.10}$$

From Equation 6.10 we can see that for a higher depth and lower friction, the surface pressure gradient decreases along the channel, also observed in the surface comparison in Figure 16b. While there is a reduced frictional effect for both the second scenario and current bathymetry during high tide, it becomes dominant during ebb tide for the shallower conditions and increases the surface slope (Figure 16a).

6.2 | Implications for the sediment transport and overall marsh erosion

The asymmetry parameters such as the peak current asymmetry, $\gamma_0(U)$ and the slack water asymmetry $\gamma_0(U_t)$ shown in Table 1-2 are commonly used as a proxy for coarse and fine sediment transport respectively when the in-situ sediment measurements are not available (Guo et al., 2019). As sediment transport is proportional to the cubic power function of flow velocity (Nidzieko and Ralston, 2012), $\gamma_0(U)$ can be an indicator of the coarse sediment import/export from the system. Similarly, $\gamma_0(U_t)$ can represent the fine sediment transport as the settling lag primarily depends on the duration difference of high water and low water slack. If we consider the flood currents are positive, $\gamma_0(U_t) > 0.0$ represents a longer high water slack and net landward transport. Comparing slack water asymmetry for Scenario 1 at different inlet and interior gauge locations show that the net fine sediment transport is toward the landward direction. Interestingly, the Leipsic River and Dock gauges show ebb dominant peak velocity skewness and favor seaward transport of the coarse materials. The new inlet opening, Sluice Ditch, has flipped the fine sediment transport from the marsh interior seaward favoring net export via the same inlet where now $\gamma_0(U_t) < 0.0$. The peak velocity skewness $\gamma_0(U)$ in Table 1 also shows an increase in seaward transport of the coarse sediment. These asymmetry parameters $\gamma_0(U)$ and $\gamma_0(U_t)$ suggest that the changes in net circulation from the artificial inlet opening has changed the overall distribution of sediment transport. We can relate this result with the observed internal marsh erosion and channel deepening inside the BHNWR. With the present bathymetry and deeper channels, the system shows a spatially varying response for both $\gamma_0(U)$ and $\gamma_0(U_t)$. While at the major inlets, Leipsic River and Sluice Ditch, the peak velocity skewness shows less ebb dominance, the slack water asymmetry shows the opposite and more ebb dominant condition for the seaward export of the fine sediments. Simultaneously, the marsh interior gauge Leatherberry displays an increase in ebb dominance for slack water asymmetry. Moreover, we have also calculated the tide-averaged U^3 that can estimate the tidally averaged sediment transport (Van der Molen, 2000). Figure 17 show the changes in tide-averaged U^3 for different morphology scenarios during both spring and neap tide cycles. It is evident that the artificial channel opening is responsible for changes in the dominant direction of sediment transport. For scenario 1, the marsh interior shows a coarse sediment import zone, which turned into an export zone after introducing the channel in scenario 2 for both spring and neap conditions. In contrast, the Woodland Beach inlet entrance at the north end of the marsh shows an increase in flood dominance and import of coarse sediment, especially during the neap cycle. Aside from the seaward directed transport, the changes in the tide range can also be a contributing factor for the marsh biomass loss and interior platform degradation. Figure 13a and Figure 14a (Leatherberry) show the marsh interior tidal range changes where the water level has decreased more during low tide from the artificially dredged channel. The duration asymmetry parameter $\gamma(\eta_t)$ in Leatherberry in Tables 1 and 2 further displays the considerable changes in the duration of rising and falling water in the marsh interior. The changes in inundation depth and period along with the starvation of the fine sediments from channels can negatively affect the evolution of the marsh elevation, ultimately destabilizing the system's balance over the years.

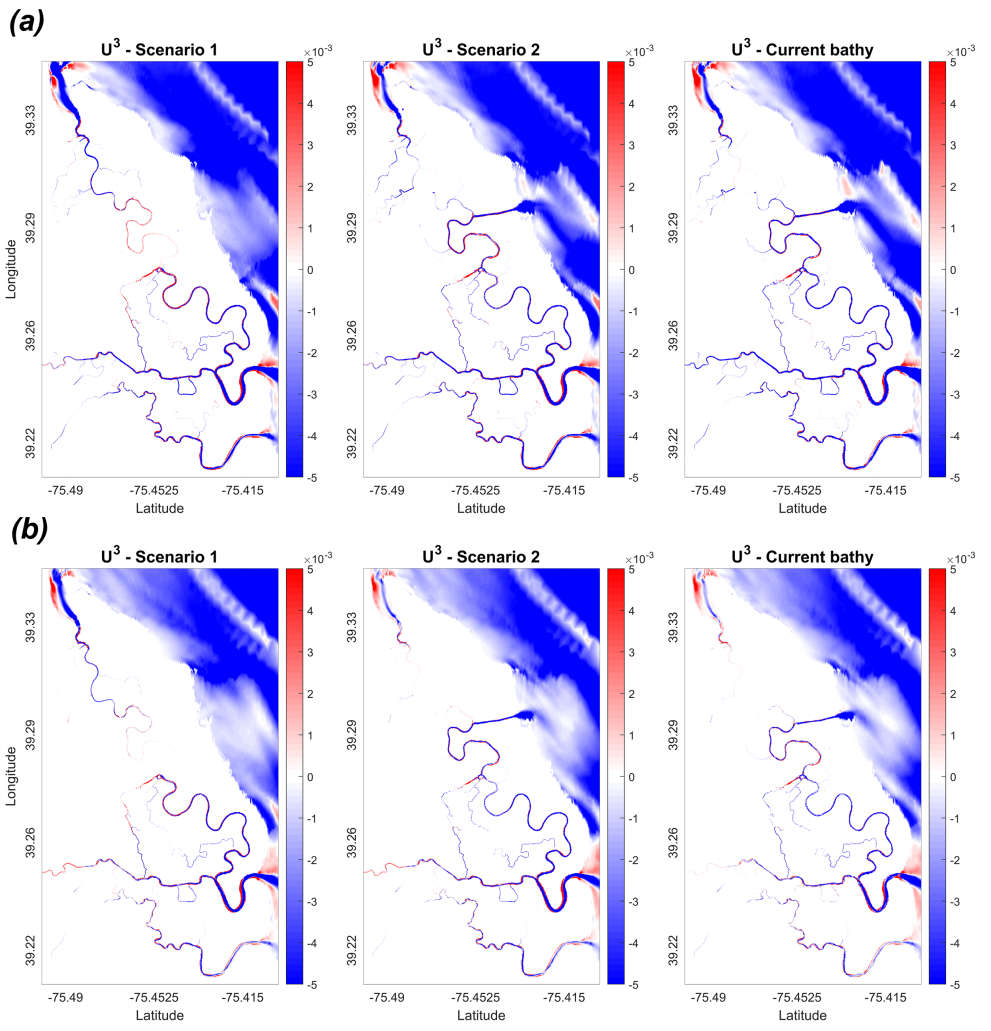

FIGURE 17 Spatial changes in tide-averaged U^3 for different morphology scenarios (a) during a spring tide cycle; (b) during a neap tide cycle. Here, positive and negative values of U^3 residual represents flood and ebb dominance respectively.

7 | CONCLUSIONS

This paper is the first step toward looking into various physical processes that had possibly accelerated the erosive nature of BHNWR wetland. We have investigated the role of the short and long-term historical bathymetry changes in altering the system's overall tidal volume exchange, and how an abrupt change in the multi-inlet circulation can affect the flow asymmetry and net sediment transport. To accurately assess the hydrodynamics in a complex system like BHNWR, a high-resolution unstructured grid model was required that represents complicated geometrical features of the wetland, and has a robust wetting/drying scheme. We chose the FVCOM model for this study due to its well-proven efficiency in resolving complex coastal geometry.

A good agreement is observed between model and in-situ point source observations in terms of water surface elevation within Delaware Bay, main interior channels, tidal flats, and over marsh platform. Moreover, the current velocity comparison in two major channels supported model reliability in predicting flood/ebb tide during normal conditions. The present state of tidal asymmetry based on channel velocity and inlet flux indicates that the system is strongly ebb dominant. The bathymetry scenario analysis and simple mechanistic explanations provided an insight on the effect of man-made channel construction in altering overall wetland hydrodynamics, and how the system became more ebb dominant due to the changes in volume exchange. The artificial connection is observed to decrease the characteristic frequency of the frictional dissipation in the channel and increase the system's natural frequency. Subsequently, the progressive channel deepening over the year has also reduced the system's overall frictional dominance. This reduced frictional regime has increased the marsh interior tide range where the mean low water elevation has increased more. The asymmetry parameters such as the slack water asymmetry estimated at the inlet entrances and marsh interior show a reversal in the net fine sediment transport direction from bathymetry changes, from landward to a more seaward export. The increase in tide range and the net seaward sediment transport are detrimental for the marsh stability and could be among the essential processes responsible for the ongoing erosion. Moreover, the skewness calculations have also demonstrated that the tide-induced circulation primarily controls the inlet asymmetry in BHNWR, and the mean residual is sensitive to both short and long-term channel bathymetry changes.

Although our current model setup can resolve the tidal hydrodynamics in extremely shallow and complex parts of the wetland, some other major processes still require attention for modeling the system's morphological evolution. An improved 2D-3D coupled modeling framework is needed in the future where the model will resolve the higher resolution vertical layers in the channel and only the depth-averaged quantities on the marsh surface. In addition, extending the current setup to a coupled hydrodynamic and wind-wave model and in-situ concentration measurements at the inlet entrances would help to better estimate the sediment exchange between the wetland and the Bay. As the BHNWR is one of the largest wetland systems in the U.S. mid-Atlantic region, the study, even with the current set of limitations, has provided valuable insights for vulnerability assessment of other major multi-inlet wetland systems worldwide.

Acknowledgements

This work has been supported by the National Fish and Wildlife Foundation and the US Department of the Interior under Grant No. 43752 to the University of Delaware, and by Delaware Sea Grant program award R/HCE-22 and RRCE-12. The authors acknowledge Christopher Sommerfield for providing the channel bathymetry data sets; Andre Rodrigues and Tobias Kukulka for large scale ROMS simulation outputs, and Dan Stotts, Laura Mitchell and Curtis George from the United States Fish and Wildlife Service for their great help and contribution during field campaigns. Also, we would like to thank the anonymous reviewers for their valuable comments, which significantly improved the content of this paper. The findings and conclusions in this article are those of the author(s) and do not necessarily represent the views of the National Fish and Wildlife Foundation, and the U.S. Fish and Wildlife Service. This research was also supported in part through the use of Information Technologies (IT) resources at the University of Delaware, specifically the high-performance computing resources.

Data Availability Statement

The shared drive access to the large-size field and model data is available from James T. Kirby (kirby@udel.edu) upon reasonable request.

references

Aretxabaleta, A. L., Ganju, N. K., Butman, B. and Signell, R. P. (2017) Observations and a linear model of water level in an interconnected inlet-bay system. *Journal of Geophysical Research: Oceans*, **122**, 2760–2780.

Aubrey, D. G. and Speer, P. E. (1985) A Study of Non-linear Tidal Propagation in shallow inlet / estuarine systems Part I : Observations. *Estuarine, Coastal and Shelf Science*, **21**, 185–205.

Becherer, J., Stacey, M. T., Umlauf, L. and Burchard, H. (2015) Lateral circulation generates flood tide stratification and estuarine exchange flow in a curved tidal inlet. *Journal of Physical Oceanography*, **45**, 638–656.

Bowman, W. (2014) Tidal wetlands trends and conditions assessment, long island. sound update. *Newsletter of the Long Island Sound Study. Winter*, **2015**.

Chen, C., Beardsley, R. C., Cowles, G., Qi, J., Lai, Z., Gao, G., Stuebe, D., Liu, H., Xu, Q., Xue, P., Ge, J., Hu, S., Ji, R., Tian, R., Huang, H., Wu, L., Lin, H., Sun, Y. and Zhao, L. (2013) An unstructured grid, finite-volume community ocean model FVCOM user manual (3rd edition). *Tech. Rep. MITSG 12-25*, Sea Grant College Program, Massachusetts Institute of Technology.

Chen, C., Qi, J., Li, C., Beardsley, R. C., Lin, H., Walker, R. and Gates, K. (2008) Complexity of the flooding/drying process in an estuarine tidal-creek salt-marsh system: An application of FVCOM. *Journal of Geophysical Research: Oceans*, **113**.

Chen, J. L., Ralston, D. K., Geyer, W. R., Sommerfield, C. K. and Chant, R. J. (2018) Wave Generation, Dissipation, and Disequilibrium in an Embayment With Complex Bathymetry. *Journal of Geophysical Research: Oceans*, **123**, 7856–7876.

Chuang, W.-S. and Swenson, E. M. (1981) Subtidal Water level variations in Lake Pontchartrain, Louisiana. *Journal of Geophysical Research*, **86**, 4198.

Deb, M., Abdolali, A., Kirby, J. T. and Shi, F. (2018a) Hydrodynamics, sediment transport and wind waves in an eroding salt marsh environment. Bombay Hook National Wildlife Refuge, Delaware. *Research Report CACR-18-04*, Center for Applied Coastal Research, Department of Civil and Environmental Engineering, University of Delaware, Newark, DE.

Deb, M., Abdolali, A., McDowell, C., Kirby, J. T., Sommerfield, C. K. and Shi, F. (2018b) Hydrodynamic, survey and sediment data collection. Bombay Hook National Wildlife Refuge, Delaware. *Research Report CACR-18-03*, Center for Applied Coastal Research, Department of Civil and Environmental Engineering, University of Delaware, Newark, DE.

Deb, M., Kirby, J. T., Shi, F. and Abdolali, A. (2020) Tidal hydrodynamics in a multi-inlet wetland system: Toward improved modeling of salt marsh flooding and draining. *Research Report CACR-20-04*, Center for Applied Coastal Research, Department of Civil and Environmental Engineering, University of Delaware, Newark, DE.

Dohner, S., Trembanis, A. and Miller, D. (2016) A tale of three storms: Morphologic response of Broadkill Beach, Delaware, following superstorm Sandy, Hurricane Joaquin, and winter storm Jonas. *Shore & Beach*, **84**, 3.

Donda, F., Brancolini, G., Tosi, L., Kovačević, V., Baradello, L., Gačić, M. and Rizzetto, F. (2008) The ebb-tidal delta of the venice lagoon, italy. *The Holocene*, **18**, 267–278. URL: https://doi.org/10.1177/0959683607086765.

Dozier, H. L. (1947) Salinity as a factor in atlantic coast tidewater muskrat production. In *North American Wildlife Conference Transactions*, vol. 12, 398–420.

Dronkers, J. (1986) Tidal asymmetry and estuarine morphology. *Netherlands Journal of Sea Research*, **20**, 117–131.

EPA (2010) Coastal Wetlands Initiative: Mid-Atlantic Review. *Tech. rep.*

Familkhalili, R. and Talke, S. A. (2016) The effect of channel deepening on tides and storm surge: A case study of Wilmington, NC. *Geophysical Research Letters*, **43**, 9138–9147.

Ferrarin, C., Tomasin, A., Bajo, M., Petrizzo, A. and Umgiesser, G. (2015) Tidal changes in a heavily modified coastal wetland. *Continental Shelf Research*, **101**, 22–33. URL: https://www.sciencedirect.com/science/article/pii/S0278434315000837.

Friedrichs, C. T. (2010) Barotropic tides in channelized estuaries. *Contemporary Issues in Estuarine Physics*, 27–61.

Friedrichs, C. T. and Madsen, O. S. (1992) Nonlinear diffusion of the tidal signal in frictionally dominated embayments. *Journal of Geophysical Research*, **97**, 5637.

Guo, L., Brand, M., Sanders, B. F., Foufoula-Georgiou, E. and Stein, E. D. (2018) Tidal asymmetry and residual sediment transport in a short tidal basin under sea level rise. *Advances in Water Resources*, **121**, 1–8.

Guo, L., Wang, Z. B., Townend, I. and He, Q. (2019) Quantification of tidal asymmetry and its nonstationary variations. *Journal of Geophysical Research: Oceans*, **124**, 773–787. URL: https://agupubs.onlinelibrary.wiley.com/doi/abs/10.1029/2018JC014372.

Hartig, E. K., Gornitz, V., Kolker, A., Mushacke, F. and Fallon, D. (2002) Anthropogenic and climate-change impacts on salt marshes of jamaica bay, new york city. *Wetlands*, **22**, 71–89.

Hsu, T. J., Chen, S. N. and Ogston, A. S. (2013) The landward and seaward mechanisms of fine-sediment transport across intertidal flats in the shallow-water region-A numerical investigation. *Continental Shelf Research*, **60**, S85–S98. URL: http://dx.doi.org/10.1016/j.csr.2012.02.003.

Huang, H., Chen, C., Blanton, J. O. and Andrade, F. A. (2008) A numerical study of tidal asymmetry in Okatee Creek, South Carolina. *Estuarine, Coastal and Shelf Science*, **78**, 190–202.

Kearney, M. S., Rogers, A. S., Townshend, J. R., Rizzo, E., Stutzer, D., Stevenson, J. C. and Sundborg, K. (2002) Landsat imagery shows decline of coastal marshes in chesapeake and delaware bays. *Eos, Transactions American Geophysical Union*, **83**, 173–178.

Kirwan, M. L. and Guntenspergen, G. R. (2010) Influence of tidal range on the stability of coastal marshland. *Journal of Geophysical Research: Earth Surface*, **115**. URL: https://agupubs.onlinelibrary.wiley.com/doi/abs/10.1029/2009JF001400.

Kirwan, M. L. and Murray, A. B. (2007) A coupled geomorphic and ecological model of tidal marsh evolution. *Proceedings of the National Academy of Sciences of the United States of America*, **104**, 6118–6122.

Kukulka, T., Jenkins III, R. L., Kirby, J. T., Shi, F. and Scarborough, R. W. (2017) Surface wave dynamics in Delaware Bay and its adjacent coastal shelf. *Journal of Geophysical Research: Oceans*, **122**, 8683–8706.

Li, Z. and Hodges, B. R. (2019) Model instability and channel connectivity for 2D coastal marsh simulations. *Environmental Fluid Mechanics*, **19**, 1309–1338.

Luettich Jr, R. A., Westerink, J. J. and Scheffner, N. W. (1992) ADCIRC: An Advanced Three-Dimensional Circulation Model for Shelves, Coasts, and Estuaries. Report 1. Theory and Methodology of ADCIRC-2DDI and ADCIRC-3DL. *Tech. rep.*, Coastal engineering research center Vicksburg MS.

Mariotti, G. and Fagherazzi, S. (2010) A numerical model for the coupled long-term evolution of salt marshes and tidal flats. *Journal of Geophysical Research: Earth Surface*, **115**.

McDowell, C. and Sommerfield, C. K. (2016) Geomorphic analysis of Bombay Hook NWR. Wilmington, DE: Delaware Wetlands Conference.

Van der Molen, J. (2000) A 2DH numerical model of tidally induced sand transport in the southern North Sea. *Interactions between estuaries coastal seas and shelf seas. Terra Scientific, Tokyo*, 265–285.

Mudd, S. M., Fagherazzi, S., Morris, J. T. and Furbish, D. J. (2013) *Flow, sedimentation, and biomass production on a vegetated salt marsh in South Carolina: Toward a predictive model of marsh morphologic and ecologic evolution*, chap. 9, 165–188. American Geophysical Union (AGU).

Nardin, W., Lera, S. and Nienhuis, J. (2020) Effect of offshore waves and vegetation on the sediment budget in the virginia coast reserve (va). *Earth Surface Processes and Landforms*, **45**, 3055–3068.

Nidzieko, N. J. and Ralston, D. K. (2012) Tidal asymmetry and velocity skew over tidal flats and shallow channels within a macrotidal river delta. *Journal of Geophysical Research: Oceans*, **117**, 1–17.

Orescanin, M. M., Elgar, S. and Raubenheimer, B. (2016) Changes in bay circulation in an evolving multiple inlet system. *Continental Shelf Research*, **124**, 13–22.

Parker, B. B. (1984) Friction Effects on the Tidal Dynamics of a Shallow Estuary. *John Hopkins University, PhD Thesis*, 292.

Pawlowicz, R., Beardsley, B. and Lentz, S. (2002) Classical tidal harmonic analysis including error estimates in MATLAB using T_TIDE. *Computers & Geosciences*, **28**, 929–937.

Picado, A., Dias, J. M. and Fortunato, A. B. (2010) Tidal changes in estuarine systems induced by local geomorphologic modifications. *Continental Shelf Research*, **30**, 1854–1864. URL: https://www.sciencedirect.com/science/article/pii/S0278434310002694.

Ralston, D. K., Geyer, W. R., Traykovski, P. A. and Nidzieko, N. J. (2013) Effects of estuarine and fluvial processes on sediment transport over deltaic tidal flats. *Continental Shelf Research*, **60**, S40–S57.

Ralston, D. K., Talke, S., Geyer, W. R., Al-Zubaidi, H. A. and Sommerfield, C. K. (2019) Bigger Tides, Less Flooding: Effects of Dredging on Barotropic Dynamics in a Highly Modified Estuary. *Journal of Geophysical Research: Oceans*, **124**, 196–211.

Ramsey, K. and Reilly, M. J. (2002) The Hurricane of October 21-24, 1878. *Delaware Geological Survey Special Publication*, **22**, 90.

Rinaldo, A., Fagherazzi, S., Lanzoni, S., Marani, M. and Dietrich, W. E. (1999) Tidal networks: 3. landscape-forming discharges and studies in empirical geomorphic relationships. *Water Resources Research*, **35**, 3919–3929.

Rodrigues, A. P. F. (2016) *Hydrodynamic modeling of Delaware Bay with applications to storm surges and coastal flooding: Current conditions and future scenarios*. Master of science in marine studies, University of Delaware, College of Earth, Ocean and Environment.

Runion, K. D. (2019) *Variability of sediment transport at a tidal wetland restoration site: Prime Hook National Wildlife Refuge, Delaware*. Master's thesis, University of Delaware.

Speer, P. E. (1984) *Tidal distortion in shallow estuaries*. Ph.D. thesis, MIT/WHOI.

Speer, P. E., Aubrey, D. G. and Friedrichs, C. T. (1991) Nonlinear hydrodynamics of shallow tidal inlet/bay systems. *Tidal hydrodynamics*, 321–339.

Stammerman, R. (2013) *Hydrodynamics and sediment transport studies in tidal marshes of the Delaware Bay using high resolution numerical models*. Ph.D. thesis, Drexel University.

Stedman, S.-M. and Dahl, T. E. (2008) Status and trends of wetlands in the coastal watersheds of the eastern United States, 1998 to 2004. *Tech. rep.*, National Oceanic and Atmospheric Administration, National Marine Fisheries Service and U.S. Department of the Interior, Fish and Wildlife Service.

United States. Army. Corps of Engineers (1910) *Report of the Chief of Engineers, U.S. Army*. No. pt. 1. U.S. Government Printing Office. URL: `https://books.google.com/books?id=eqVAAQAAMAAJ`.

Watson, E. B., Wigand, C., Davey, E. W., Andrews, H. M., Bishop, J. and Raposa, K. B. (2017) Wetland loss patterns and inundation-productivity relationships prognosticate widespread salt marsh loss for southern new england. *Estuaries and Coasts*, **40**, 662–681.

Williams, S. J. (1995) Louisiana coastal wetlands: A resource at risk. *Tech. rep.*, US Geological Survey.

Supplemental Materials

8 | FVCOM VERTICALLY INTEGRATED MOMENTUM EQUATION

The original FVCOM 2D vertically integrated, barotropic mode, x-momentum equation (Chen et al., 2013) is

$$\frac{\partial \bar{u} H}{\partial t} = \underbrace{-\frac{\partial \bar{u}^2 H}{\partial x} - \frac{\partial \bar{u}\bar{v} H}{\partial y}}_{\text{ADV}} + f\bar{v}H \underbrace{- gH\frac{\partial \eta}{\partial x}}_{\text{DP}} - \underbrace{\tau_{bx}}_{\text{FRIC}} + \underbrace{H\tilde{F}_x}_{\text{Diff}} + G_x \tag{8.1}$$

where x and y are the east and north axes of the Cartesian coordinate; $\bar{u}$ and $\bar{v}$ are the depth-averaged x, y velocity components; η is surface elevation, $H = h + \eta$ is total water depth, and τ_{bx} is the x component of bottom stress. The difference between nonlinear terms based on vertically-averaged 2-D variables and terms resulting from vertical integration of 3-D variables are given by G_x defined by (Chen et al., 2013)

$$G_x = \frac{\partial \bar{u}^2 H}{\partial x} + \frac{\partial \bar{u}\bar{v} H}{\partial y} - H\tilde{F}_x - \left[\frac{\partial \overline{u^2} H}{\partial x} + \frac{\partial \overline{uv} H}{\partial y} - H\overline{F}_x\right] \tag{8.2}$$

where

$$H\tilde{F}_x \approx \frac{\partial}{\partial x}\left[2\bar{A}_m H \frac{\partial \bar{u}}{\partial x}\right] + \frac{\partial}{\partial y}\left[\bar{A}_m H \left(\frac{\partial \bar{u}}{\partial y} + \frac{\partial \bar{v}}{\partial x}\right)\right] \tag{8.3}$$

$$H\overline{F}_x \approx \frac{\partial}{\partial x}\overline{2A_m H \frac{\partial u}{\partial x}} + \frac{\partial}{\partial y}\overline{A_m H\left(\frac{\partial u}{\partial y} + \frac{\partial v}{\partial x}\right)} \tag{8.4}$$

Here, A_m is the horizontal eddy diffusion coefficient and the overline $\overline{(\cdot)}$ denotes the depth-averaged value.

9 | MODEL VALIDATION: HURRICANE SANDY 2012 AND HURRICANE JOAQUIN 2015

We looked into surface elevation time series during Hurricane Sandy and Hurricane Joaquin at Delaware Bay NOAA tide gauge location (Figure A1). The model skill is 0.99 for both events, and the negative sign on the low average bias index value represents a slight under-prediction by the model. We can see that the subtidal correction is much more accurate for Hurricane Joaquin compared to Hurricane Sandy, and has a smaller bias during the main surge event. The comparison at the BHNWR tide gauges is shown in Figure A2 for Hurricane Sandy, again revealing higher model skill at the tide gauge close to the Bay (Navigation Light). It shows an increase in the scatter at interior channel gauges when surge inundates the entire marsh platform. Some distinct scatter appears in all the interior gauges during one specific tidal cycle at the end of the surge, where the model overestimates surface elevation and also develops a phase lag due to gradual draining from the marsh platform. Water surface elevation is collected along a transect on the marsh surface throughout the year 2015, using HOBO water level loggers. Locations of the HOBO gauges in the marsh are shown in Figure 2. The FVCOM model results are compared with in-situ data for Hurricane Joaquin at the four DNREC tide gauges (Figure A3) and on the marsh surface (Figure A4). A better model performance compared to the case of Hurricane Sandy is observed in three of the gauges, mainly at Navigation Light (close to the Bay), Leatherberry and Shearness (located in the marsh interior). This could be due to a more accurate representation of the sub-tidal forcing at the boundaries and the channel bathymetry surveyed during the year 2015. Model skill and correlation score demonstrate a good agreement where both are close to 0.99. At Dock, we observed a significant deviation during falling tide (Figure A3, last subplot), also evident from the model correlation and skill that decreases to 0.96 and 0.95 respectively. The estimated regression slope and averaged bias index value show model over-estimation, that is mainly coming from a higher phase lag. The similar trend can be also noticed in longer-term comparison we have shown earlier.

The results at the six HOBO stations presented in Figure A4 show that FVCOM does a reasonable job of predicting maximum inundation depths over the marsh platform. However, the model was seen to exhibit one particular problem during marsh draining phase, artificial ponding, where an extra water storage is apparent for the entire time at HOBO location 3 to 6. The complex topographic features such as rills and cuts through channel berms and small creeks on the marsh platform are often missing in the model grid due to incomplete resolution in data sources such as LiDAR and the loss of resolution in the development of DEM's and model grids. Many of these small-scale features stay hidden under dense vegetation canopies and are thus not easily recognized using even higher resolution techniques. This marsh drainage problem is significant when severe surges are under consideration and required an entirely separate study to quantify the total error and proposing a solution, described in more detail in Deb et al. (2020). It is a universal issue for the coastal wetland modeling community and still an active matter of research. We need more field data sets from hydraulically isolated depressions in BHNWR to correctly resolve the entire marsh platform flooding and draining. For this study, we chose M2 and S2 forcing only to limit the isolated low-spot submergence over the marsh platform and represent a simplistic condition of the regular wetland flooding and draining. Our assessment of the wetland tidal hydrodynamics and asymmetry described in the results and discussion is not affected by the pooling shown in Figure A4.

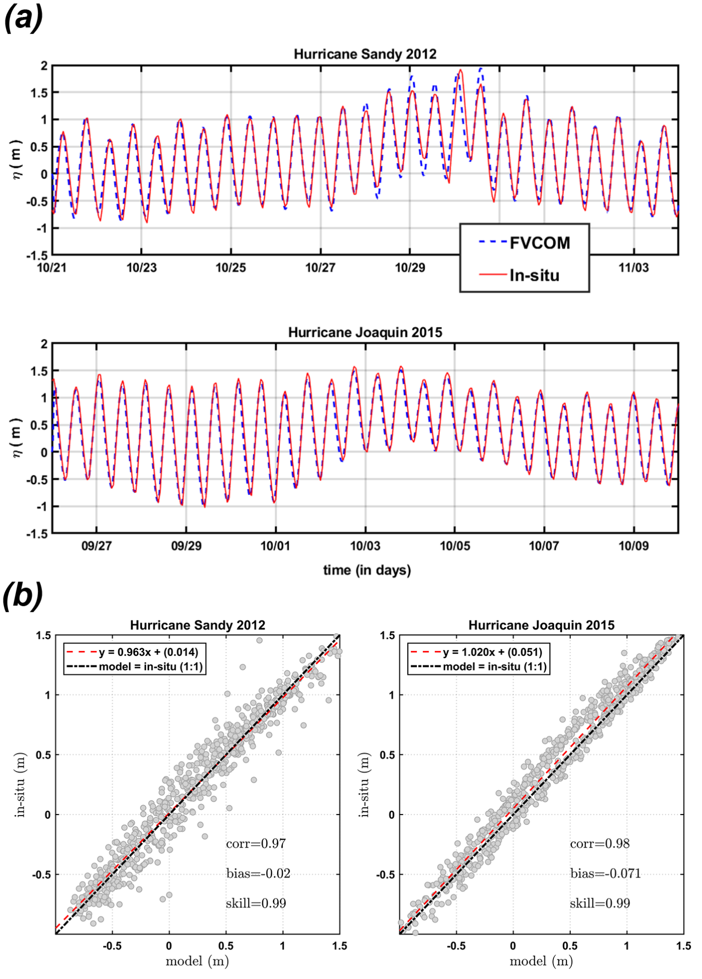

FIGURE A1 (a) Comparison between FVCOM model (in blue) and in-situ (in red) water surface elevation during Hurricane Sandy, 2012 and Hurricane Joaquin, 2015 at Ship John Shoal NOAA tide gauge in the Delaware Bay (in meters, from NAVD88 vertical reference level); (b) Scatter comparison (correlation, average bias index and skill) between FVCOM model and in-situ water surface elevation at the same gauge.

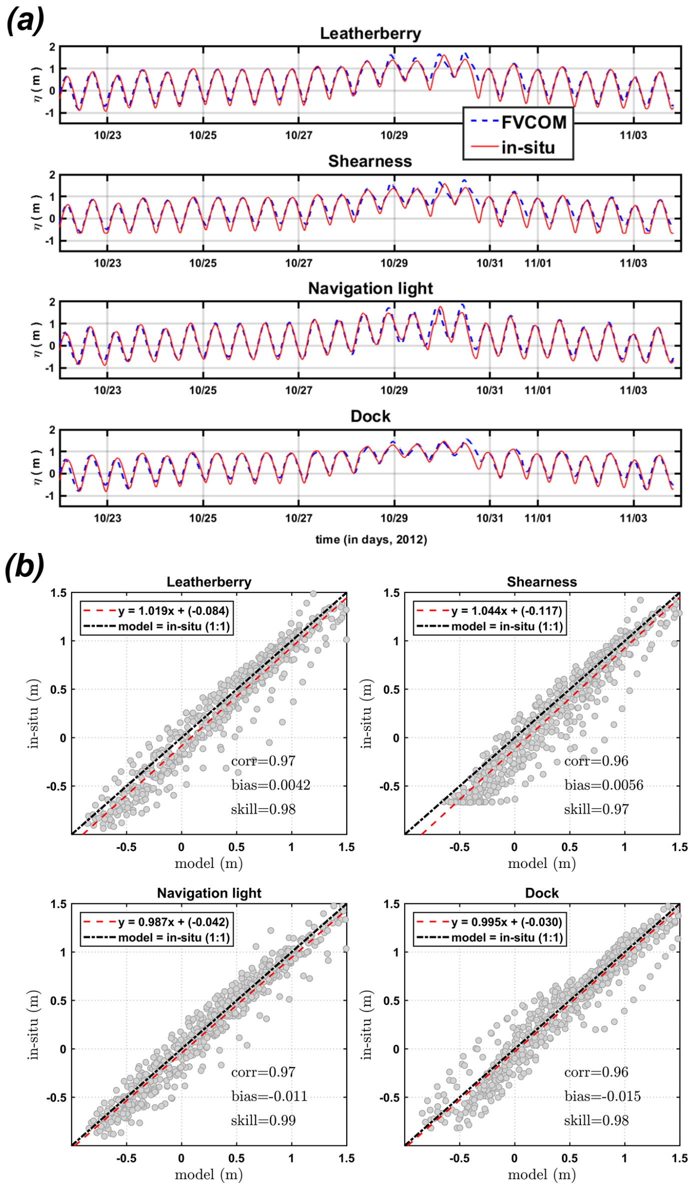

FIGURE A2 (a) Comparison between FVCOM model (in blue) and in-situ (in red) water surface elevation during Hurricane Sandy, 2012 at different DNREC tide gauges (in meters, from NAVD88 vertical reference level); (b) Scatter comparison (correlation, average bias index and skill) between FVCOM model and in-situ water surface elevation at the same gauges.

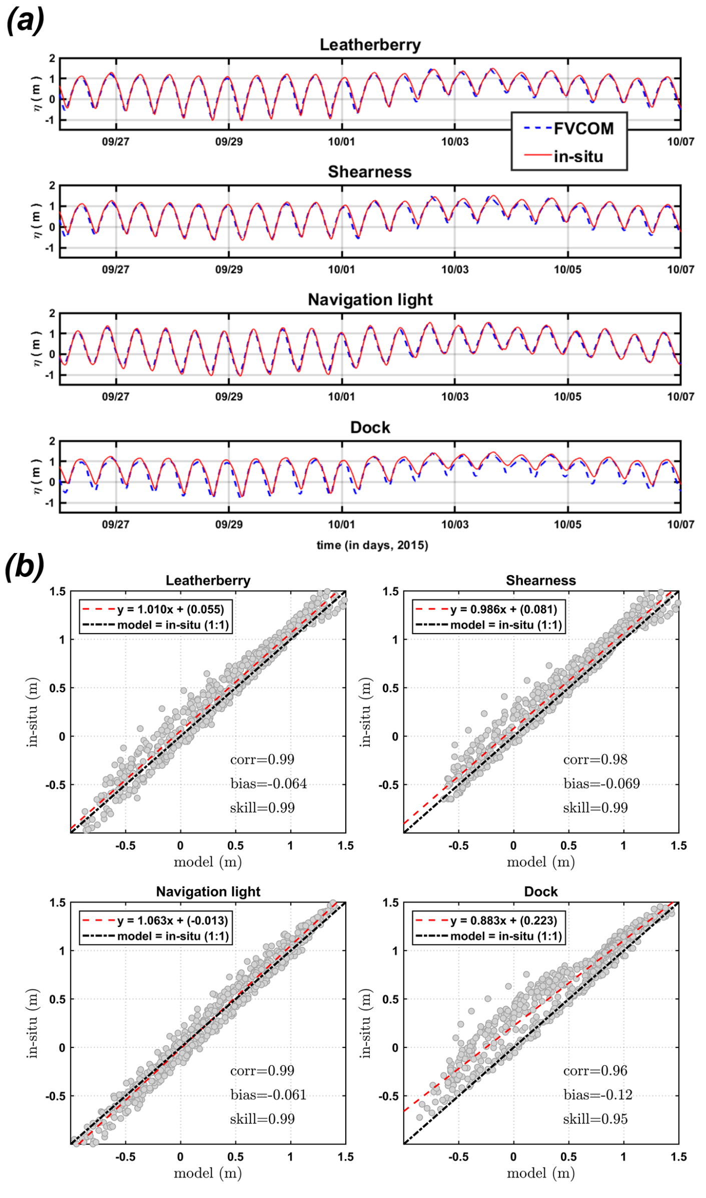

FIGURE A3 (a) Comparison between FVCOM model (in blue) and in-situ (in red) water surface elevation during Hurricane Joaquin, 2015 at different DNREC tide gauges (in meters, from NAVD88 vertical reference level); (b) Scatter comparison (correlation, average bias index and skill) between FVCOM model and in-situ water surface elevation at the same gauges.

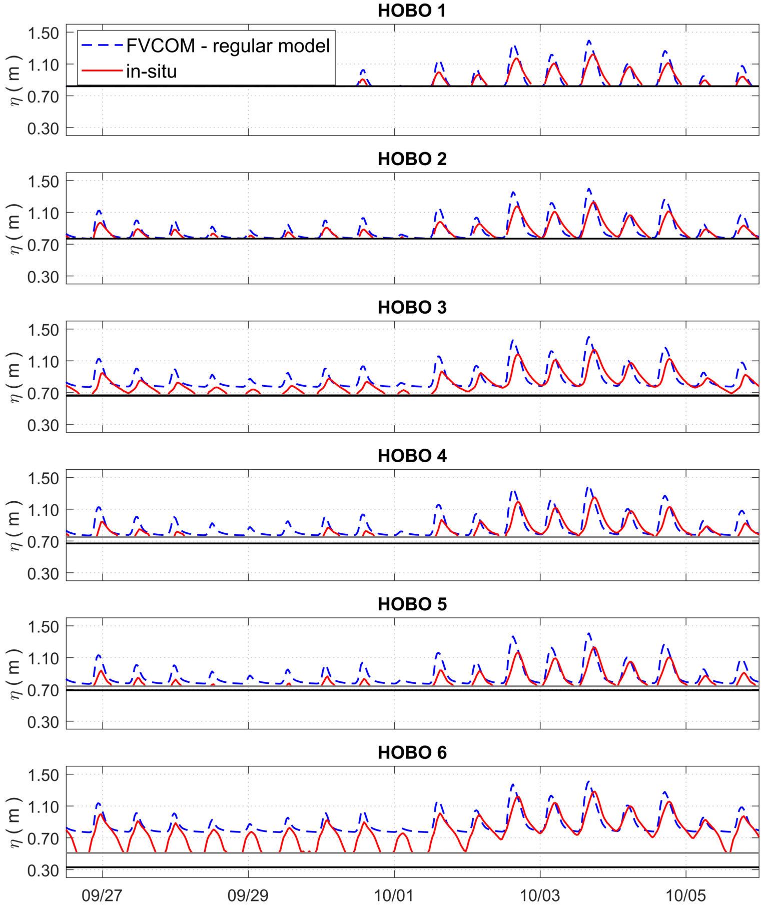

FIGURE A4 Comparison between FVCOM model (in blue) and in-situ (in red) water surface elevation during Hurricane Joaquin, 2015 at different HOBO gauge locations (in meters, from NAVD88 vertical reference level). The black straight and gray lines represent model grid bottom and surveyed elevation.

10 | NOTATIONS

TABLE 1 Description and unit of different variables used in the analysis

variable	description	unit
γ_0	Asymmetry parameter	dimensionless
U	Principal velocity component	m/s
U_{mr}	Mean-removed principal velocity component	m/s
Q	Volume flux	m^3/s
Q_{mr}	Mean-removed volume flux	m^3/s
η	Water surface elevation	m
L	Channel length	m
W	Channel width	m
h	Channel mean water depth	m
C_d	drag coefficient	dimensionless
r	linear drag coefficient	m/s